International Journal of Pharmaceutics 650 (2024) 123659

Contents lists available at ScienceDirect

International Journal of Pharmaceutics

journal homepage: www.elsevier.com/locate/ijpharm

Rational approach to design gold nanoparticles for photothermal therapy: the effect of gold salt on physicochemical, optical and biological properties

Tânia Ferreira-Gonçalves [a,b], Daniela Nunes [c], Elvira Fortunato [c], Rodrigo Martins [c], António P. de Almeida [d], Lina Carvalho [e], David Ferreira [f], José Catarino [g,h], Pedro Faísca [g,h], Hugo A. Ferreira [b], M. Manuela Gaspar [a], João M.P. Coelho [b], Catarina Pinto Reis [a,b,*]

[a] Research Institute for Medicines (iMed.ULisboa), Faculty of Pharmacy, Universidade de Lisboa, Av. Professor Gama Pinto, 1649-003 Lisboa, Portugal
[b] Instituto de Biofísica e Engenharia Biomédica, Faculdade de Ciências, Universidade de Lisboa, Campo Grande, 1749-016 Lisboa, Portugal
[c] Department of Materials Science, NOVA School of Science and Technology, Campus de Caparica, i3N/CENIMAT, 2829-516 Caparica, Portugal
[d] Faculdade de Medicina Veterinária, Universidade de Lisboa, Av. Universidade Técnica, 1300-477 Lisboa, Portugal
[e] Central Testing Laboratory, University of Aveiro, Campus Universitário de Santiago, 3810-193 Aveiro, Portugal
[f] Comprehensive Health Research Centre (CHRC), Departamento de Medicina Veterinária, Escola de Ciências e Tecnologia, Universidade de Évora, Pólo da Mitra, Ap. 94, 7002-594 Valverde, Évora, Portugal
[g] Faculdade de Medicina Veterinária, Universidade Lusófona de Humanidades e Tecnologias, Campo Grande 376, 1749-024 Lisboa, Portugal
[h] CBIOS-Research Center for Biosciences & Health Technologies, Universidade Lusófona de Humanidades e Tecnologias, Campo Grande 376, 1749-024 Lisboa, Portugal

ARTICLE INFO

Keywords:
Nanomedicine
Pharmaceutical Nanotechnology
Manufacture and evaluation
Gold Nanoparticles
Photothermal Therapy

ABSTRACT

Among the unique characteristics associated to gold nanoparticles (AuNPs) in biomedicine, their ability to convert light energy into heat opens ventures for improved cancer therapeutic options, such as photothermal therapy (PTT). PTT relies on the local hyperthermia of tumor cells upon irradiation with light beams, and the association of AuNPs with radiation within the near infrared (NIR) range constitutes an advantageous strategy to potentially improve PTT efficacy. Herein, it was explored the effect of the gold salt on the AuNPs' physicochemical and optical properties. Mostly spherical-like negatively charged AuNPs with variable sizes and absorbance spectra were obtained. In addition, photothermal features were assessed using *in vitro* phantom models. The best formulation showed the ability to increase their temperature in aqueous solution up to 19 °C when irradiated with a NIR laser for 20 min. Moreover, scanning transmission electron microscopy confirmed the rearrangement of the gold atoms in a face-centered cubic structure, which further allowed to calculate the photothermal conversion efficiency upon combination of theoretical and experimental data. AuNPs also showed local retention after being locally administered in *in vivo* models. These last results obtained by computerized tomography allow to consider these AuNPs as promising elements for a PTT system. Moreover, AuNPs showed high potential for PTT by resulting in *in vitro* cancer cells' viability reductions superior to 70 % once combine with 5 min of NIR irradiation.

1. Introduction

Since ancient history, gold-based materials have been widely explored in several fields, namely jewelry, exchange trade systems (such as coins), gilding and technology (Habashi, 2016; Savage, 2013). Moreover, due to its ability to exhibit different colors depending on its mixture with other elements or on the way how they interact with the light, they are also widely used in glass staining (X. Yang et al., 2015). Despite the undeniable economical and industrial value of gold-based materials, they also present high potential for biomedical and pharmaceutical applications (Sztandera et al., 2019; X. Yang et al., 2015). The oldest and long-lasting application of gold-based materials at macroscale in biomedicine relies on its integration in dentures, with the first know use dating back to the XXI century (Savage, 2013). When,

* Corresponding author.
E-mail addresses: taniag1@edu.ulisboa.pt (T. Ferreira-Gonçalves), daniela.gomes@fct.unl.pt (D. Nunes), emf@fct.unl.pt (E. Fortunato), rfpm@fct.unl.pt (R. Martins), alalmeida@fmv.ulisboa.pt (A.P. de Almeida), linamcarvalho@ua.pt (L. Carvalho), david.ferreira@uevora.pt (D. Ferreira), p5663@ulusofona.pt (J. Catarino), pedrofaisca@ulusofona.pt (P. Faísca), hugoferreira@campus.ul.pt (H.A. Ferreira), mgaspar@ff.ulisboa.pt (M.M. Gaspar), jmcoelho@fc.ul.pt (J.M.P. Coelho), catarinareis@ff.ulisboa.pt (C.P. Reis).

https://doi.org/10.1016/j.ijpharm.2023.123659
Received 24 July 2023; Received in revised form 27 November 2023; Accepted 28 November 2023
Available online 30 November 2023

transitioning to the nanoscale, the first report elaborated by Michael Faraday dates back to 1857 (Faraday, 1857), and it unveils the distinctive and unique properties of gold at nanoscale from gold at macroscale, bulk, and molecular forms, aspects further reported in many other studies (Faraday, 1857; Jeevanandam et al., 2018; X. Yang et al., 2015). Gold-based materials at nanoscale, from here forward called gold nanoparticles (AuNPs), are known by their low toxicity, exquisite electrical and optical properties, and their relatively easy synthesis and surface functionalization (Sztandera et al., 2019; Venditti, 2019; X. Yang et al., 2015). Moreover, AuNPs also present phenomenal photothermal properties, once they have the ability of converting light energy into heat (Amendola et al., 2017; Bai et al., 2020). This happens when the AuNPs are irradiated with light beams of a certain wavelength and irradiance and leds to a surface plasmon resonance (SPR) effect (Amendola et al., 2017). Altogether, these properties make AuNPs highly attractive for biomedical applications (Ferreira-Gonçalves et al., 2021). Over time, there has been an increasing research on AuNPs which has led to top edge applications for up to date daily challenges, as it was the case of their application in Covid 19 massive testing (Wang et al., 2022; Yano et al., 2022). Further applications include sensing (Jiang et al., 2018; "Luminex®," n.d.), imaging (Bouché et al., 2020; Daems et al., 2021), drug delivery (Ferreira-Gonçalves et al., 2021; Venditti, 2019; X. Yang et al., 2015), radiotherapy (Luo et al., 2019; Shrestha et al., 2016), photodynamic therapy (Niculescu and Grumezescu, 2021; Y. Yang et al., 2015) and photothermal therapy (PTT) (Nardine S Abadeer and Murphy, 2016; Amaral et al., 2021; Costa et al., 2020; Lopes et al., 2021; Riley and Day, 2017). Additionally, attending the bivalent features of AuNPs, they have also been proposed in combinatorial therapeutic systems, combining PTT for instance with chemotherapy (Park et al., 2008; Sheth et al., 2020; Urries et al., 2014), radiotherapy (X. Xu et al., 2019) and PDT (Arellano et al., 2023; Wang et al., 2019).

Properties such as size, shape, surface charge and light interaction (e.g., absorbance, scattering or reflection) of AuNPs depend greatly on the synthetic method used (Jiang et al., 2012; Venditti, 2019), and thus it must be selected in an early stage depending on the application intended for the AuNPs, as well as on the access to required equipment. AuNPs can be produced through physical (Lee et al., 2012; Naharuddin et al., 2020; Ngo et al., 2016; Shen et al., 2011), electrochemical (Huang et al., 2006; Nguyen et al., 2019; Paramasivam et al., 2017), and chemical methods (De Souza et al., 2019), among which chemical methods are the simplest and require no major technical equipment in contrast with other synthetic approaches (Ferreira-Gonçalves et al., 2021; Jiang et al., 2012). Several chemical approaches have already been reported, being the more renowned the Turkevich method (Turkevich et al., 1951), the Frens method (Frens, 1973), the Brust method (Brust et al., 1994) and seed-mediated growth method (Jana et al., 2001; Sztandera et al., 2019; Yang et al., 2015a). These methods have been widely used and adapted and result mostly in spherical-like AuNPs, except for the seed-mediated growth which allows the preparation of other shapes (Ferreira-Gonçalves et al., 2021; Yang et al., 2015a). Despite quite optimized, such methods include the use of toxic and environment harmful reagents such as citrate and cetyltrimethylammonium bromide (CTAB) (Alkilany and Murphy, 2010; Jiang et al., 2012), which has encouraged the search for more environmentally friendly approaches (Ferreira-Gonçalves et al., 2021; Ortiz-Castillo et al., 2020; Sengani et al., 2017; Slepička et al., 2020; Sztandera et al., 2019). Some of those approaches take advantage of plant extracts (Fazal et al., 2014), live organisms (Reddy et al., 2010) or even buffers (Habib et al., 2005), among others (Lee et al., 2020). Among the library of plant extracts already proposed for bio-based synthesis of AuNPs, our group proposed the use of *Plectranthus saccatus* Benth which resulted in a combination of spherical and rod-shaped AuNPs with sizes around 200 nm and preferential absorbance of radiation within the near infrared (NIR) range (Silva et al., 2016b). The proposed method arose, however, some concerns regarding the AuNP shape uniformity, apprehensions often observed for other bio-based synthetic alternative approaches (Ortiz-Castillo et al., 2020; Shankar et al., 2004). Some of the reasons possibly linked to the variability observed for plant-based alternatives can be related to possible synergetic effects of multiple constituents of plant extracts (Ortiz-Castillo et al., 2020). Thus, in order to surpass the main limitations associated to previously published methods, our group has been working on the optimization of a synthetic method in which the plant extract was replaced by its main constituent: rosmarinic acid (RA) (Rijo et al., 2012; Silva et al., 2016b). The updated method uses a combination of reducing agents of the gold salt, among which L-ascorbic and rosmarinic acids (Amaral et al., 2021; Costa et al., 2020; Ferreira-Gonçalves et al., 2022; Lopes et al., 2021). Previous results of this method report the production of mostly spherical-like negatively charged AuNPs (Amaral et al., 2021; Costa et al., 2020; Ferreira-Gonçalves et al., 2022; Lopes et al., 2021). To the best of authors knowledge, no other groups proposed the combination of such reducing agents, even though others have already proposed the independent use of RA (Lim and Park, 2018; Sarkar et al., 2010) or ascorbic acid (AA) (Larm et al., 2018; Malassis et al., 2016) as reducing agents. Groups using RA or AA for AuNPs syntheses reported the preparation of small-sized (<80 nm) AuNPs with preferential absorption of the radiation within the visible range, clearly distinguishing from the particles herein obtained.

Among the multiple biomedical applications in which AuNPs have been attracting particular attention it is photothermal therapy (Nardine S Abadeer and Murphy, 2016; Riley and Day, 2017). PTT is recognized as a minimally invasive therapy relying on the local induction of cellular hyperthermia (temperatures between 41 °C and 47 °C (Huang et al., 2008; Kumari et al., 2021)) upon irradiation with light beams (Liu et al., 2017; Zou et al., 2016), which might result in preferential death of tumor cells rather than healthy cells once they present poorer ability to dissipate heat (Pérez-Hernández, 2018). Attending the definition of PTT, it is possible to infer that its efficacy will greatly depend on two factors: 1. how deep can the light penetrate into the tissues/tumor; and 2. how much heat can be generated, once it must be high enough to damage tumor cells without affecting healthy cells, but simultaneously not too high to avoid thermal resistance of the cells (Deng et al., 2021; Yi et al., 2021). Attending the first point, light interacts differently with biological tissues depending on its wavelength (Jacques, 2013), and it was defined a therapeutic window (wavelengths between 600 and 1200 nm) (Salehpour et al., 2019; Yun and Kwok, 2017) belonging to the visible and near infrared (NIR) range, in which radiation is less absorbed and scattered by the tissues (Bashkatov et al., 2005; Park et al., 2021; Zhang et al., 2021) and thus, allows to reach deeper areas. For this reason, the use of NIR radiation allows to improve PTT potential for deeper tumors, even though it is still limited to superficial tumors (up to a few centimeters deep) (Sheng et al., 2017). As for the second point, the use of photothermal enhancers such as AuNPs has been explored and translated into promising results (Moustaoui et al., 2019; Riley and Day, 2017). As aforementioned, AuNPs have the unique ability to convert light energy into heat which is in line with the mechanism of action of PTT. With this application in mind, AuNPs were synthesized and characterized in order to present optimized features to be applied as part of a PTT system combining *in situ* administration of local particles with external irradiation with a NIR laser for breast cancer treatment.

2. Materials and methods

2.1. Materials, cell lines and cell culture

Gold (III) chloride trihydrate solution ($HAuCl_4 \cdot 3H_2O$), L-ascorbic acid (L-AA), silver nitrate ($AgNO_3$), rosmarinic acid (RA), phosphate-buffered saline (pH 7.4, PBS), dimethyl sulfoxide (DMSO), trypsin, fetal bovine serum (FBS) and 3-(4,5-Dimethylthiazol-2-yl)-2,5-Diphenyltetrazolium Bromide (MTT) were purchased from Sigma-Aldrich (St. Louis, MO, USA). Dulbecco's modified Eagle medium (DMEM) and Roswell Park Memorial Institute (RPMI) medium were supplied by Biowest (Nuaillé, France), and penicillin and streptomycin were

obtained from Invitrogen (Waltham, MA, USA). By its turn, *Artemia salina* eggs and artificial sea water salt for *artemia* growth were purchased from JBL GmbH and Co., KG (Neuhofen, Germany). Commercialized formulations of ketamine, medetomidine and atipamezole were supplied by B. Braun (Barcelona, Spain). All other reagents and solvents were of analytical purity grade. Milli-Q water was purified through a Millipore system (Millipore, Burlington, MA, USA).

In vitro efficacy of the combination of AuNPs with laser irradiation was assessed in 2D cultures of commercialized cell lines: 4T1 (murine triple-negative breast cancer cells (Schrörs et al., 2020; Yuan et al., 2016), CRL-2539™, ATCC®, Manassas, VA, USA), MCF-7 (human estrogen receptor (ER) and progesterone receptor (PR) positive and HER2 negative breast cancer cells (Ciccone et al., 2018), HTB-22™, ATCC®, Manassas, VA, USA) and HaCaT (human skin keratinocytes, HEKa PCS-200-011™, ATCC®, Manassas, VA, USA). MCF-7 and HaCaT cells were cultured in DMEM with high glucose (4500 $mg.L^{-1}$) enriched with 10 % FBS (*v/v*), 100 $IU.mL^{-1}$ penicillin and 100 $\mu g.mL^{-1}$ streptomycin (henceforward, complete medium), whereas 4T1 cells were cultured in RPMI with the same enrichment than DMEM. Cells were kept at 37 °C and 5 % CO_2 atmosphere in an incubator (NuAire NU-5500E, NuAire, Plymouth, MN, USA). Until a confluence of 80 % was reached the medium was changed every two days.

2.2. Methods

2.2.1. AuNPs syntheses

The AuNPs were synthesized using an adaptation of a method previously reported (Amaral et al., 2021; Ferreira-Gonçalves et al., 2022; Lopes et al., 2020; Silva et al., 2016b). In a previous publication the effect of the RA concentration over the AuNPs main features for a fixed concentration of $HAuCl_4{\cdot}3H_2O$ was tested. For the analyzed parameters it was found that the concentration of RA leading to best results was 3.5 mM (Ferreira-Gonçalves et al., 2022). Herein the concentration of RA was kept, and the $HAuCl_4{\cdot}3H_2O$ concentration was changed (0.1 up to 1.0 mM). The different concentrations tested, as well as the nomenclature adopted are summarized in Table 1. In the first part of the work, syntheses of 20 mL were prepared, and later, 100 mL syntheses were explored by scaling up the volumes of the reagents used. Briefly, the AuNPs were prepared based on the subsequent mixture of $HAuCl_4{\cdot}3H_2O$ with reducing agents ($AgNO_3$ (1 mM), L-AA (2 mM) and RA (3.5 mM), added in this respective order) at room temperature (RT), under magnetic stirring (800 rpm) (Heidolph MR3001, Heidolph Instruments, Schwabach, Germany) carried out for 15 min. Then, the AuNPs were protected from light and stored for 24 h at 2 °C. In order to remove unreacted reagents, AuNPs suspensions were centrifuged at 1520 × g and RT for 20 min (eppendorf 5804 R, Eppendorf, Hamburg, Germany), the supernatants were discarded, and the pellets were resuspended in Milli-Q water. At last, the colloidal AuNPs were protected from light and stored at 2 °C until being used.

2.2.2. Physicochemical characterization of AuNPs

The prepared AuNPs were primarily characterized in regards of size, polydispersity index (PdI), surface charge and maximum absorbance peak. Size, determined as hydrodynamic diameter, and polydispersity index (PdI) of AuNPs aqueous solutions (dilutions 1:10 *v/v* in Milli-Q water) were assessed by dynamic light scattering, DLS (Zetasizer Nano S, Malvern Instruments, Malvern, UK) applying a constant scattering angle of 173° and temperature of 25 °C. Data from each sample includes 3 series of 11 measurements each. Surface charge was assessed based on the zeta-potential by electrophoretic mobility (Zetasizer Nano Z, Malvern Instruments, Malvern, UK) upon dilution (1:10, *v/v*) of the samples into PBS 1× (pH 7.4, USP32). Measurements were carried out at 25 °C in 3 series of 10 measurements each. Lastly, absorbance spectra of AuNPs were obtained by spectrophotometry (Shimadzu UV-1280 Multipurpose UV–Visible Spectrophotometer, Shimadzu Europe GmbH, Duisburg, Germany) within a wavelength range from 400 nm up to 1000 nm.

Table 1
Nomenclature used to identify the AuNPs depending on the $HAuCl_4{\cdot}3H_2O$ concentration used for the syntheses.

Nomenclature	$HAuCl_4{\cdot}3H_2O$ Concentration (mM)
Core 1 AuNPs (standard protocol)	1.00
Core 2 AuNPs	0.50
Core 3 AuNPs	0.25
Core 4 AuNPs	0.10

In addition to the previous characterization, AuNPs solutions from scaled up syntheses were also analyzed by Inductively Coupled Plasma by Optical Emission Spectrometry (ICP-OES, Jobin Yvon Activa M ICP-OES, HORIBA Jobin Yvon, Kyoto, Japan) to assess the molar concentration of the syntheses in regards of Au element content. Prior analysis, each sample was digested in a closed perfluoroalkoxy (PFA) tube containing 3 mL of HCl and 1 mL of HNO_3, by subjecting the tubes to microwave radiation at 180 °C for 10 min. Next, the sample was collected, mixed with 10 mL of ultrapure water, and analyzed. Attending ICP-OES results, the Recovery Yield based on the Au content ($Recovery\ Yield_{Au}$) was determined in accordance with Equation (1),

$$Recovery\ Yield_{Au}\ (\%) = \frac{C_{Au\ atoms}}{C_{Au\ salt}} \times 100 \tag{1}$$

where, $C_{Au\ atoms}$ is the molar concentration of Au found in the AuNPs suspension quantified by ICP-OES, and $C_{Au\ salt}$ is the molar concentration of Au found in the $HAuCl_4{\cdot}3H_2O$ solution used on the AuNPs syntheses (also quantified by ICP-OES).

Once the Au concentration ($C_{Au\ atoms}$ by ICP-OES) and the diameter of the AuNPs were known, the number of Au atoms per AuNPs was estimated. Firstly, based on the predominant spherical morphology of the AuNPs, their volume (V_{AuNPs}) was determined based on Equation (2):

$$V_{AuNPs} = \frac{4}{3}\pi r^3 \qquad (nm^3) \tag{2}$$

where, r is the AuNPs' radius. It is described in the literature that Au (III) ions have a preferred coordination number of 4 (Roy et al., 2022), resulting in a face-centered cubic (FCC) crystal structure (Pu et al., 2018). Moreover, attending data from Crystallography Open Database a FCC unit cell of Au has a volume ($V_{unit\ cell}$) of 67.42 $Å^3$ ("Information card for entry 1100138," n.d.). Thus, following the reported by Pu *et al.* (Pu et al., 2018), the number of unit cells in a single AuNP ($N_{unit\ cells}$) can be calculated as:

$$N_{unit\ cells} = \frac{V_{AuNPs}}{V_{unit\ cell}} \tag{3}$$

By its turn, once Au (III) presents a preferred coordination number of 4, the number of Au atoms per AuNP ($N_{Au\ atoms}$) can be calculated by:

$$N_{Au\ atoms} = 4 \times N_{unit\ cells} \tag{4}$$

Subsequently, the molar concentration of AuNPs (C_{AuNPs}) can be estimated for a certain concentration of Au ($C_{Au\ atoms}$ by ICP-OES)(Pu et al., 2018):

$$C_{AuNPs} = \frac{C_{Au\ atoms}}{N_{Au\ atoms}} \qquad (M) \tag{5}$$

and the concentration of AuNPs per volume can also be estimated:

$$C_{AuNPs} = \frac{C_{Au\ atoms} \times \left(6.022 \times 10^{23}\right)}{N_{Au\ atoms}} \qquad (AuNPs/L) \tag{6}$$

At last, attending the Beer-Lambert law, and combining data from the AuNPs absorption at a certain wavelength (A_λ), the path length (L, corresponding to the cuvette' width) and the molar concentration of

AuNPs (C_{AuNPs}), the molar extinction coefficient (ε_λ) can be determined as:

$$\varepsilon_\lambda = \frac{A_\lambda}{L \times C_{AuNPs}} \qquad \left(M^{-1}cm^{-1}\right) \tag{7}$$

2.2.3. Morphological and elemental characterization of AuNPs

Scanning electron microscopy (SEM) images of AuNPs were acquired with a Hitachi Regulus 8220 Scanning Electron Microscope (Hitachi, Mito, Japan) equipped with an Oxford energy dispersive X-ray spectroscopy (EDS) detector (Oxford Instruments, Abingdon, Oxfordshire, England). For the analyses, 20 μL droplets of AuNPs aqueous suspensions were added to silicon substrates and allowed to attach and dry at RT.

Scanning transmission electron microscopy (STEM) observations, including high-angle annular dark-field (HAADF) imaging, were carried out with a Hitachi HF5000 field-emission transmission electron microscope operated at 200 kV (Hitachi, Mito, Japan). This is a cold field emission gun (FEG) TEM/STEM with a spherical aberration-corrector for the probe and it is equipped with one 100 mm^2 EDS detector from Oxford Instruments (Oxford Instruments, Abingdon, Oxfordshire, England). A drop of the sonicated dispersion was deposited onto lacey-carbon copper grids and allowed to dry before observation.

2.2.4. In vitro thermal activation studies using phantoms

Thermal activation studies were carried out after irradiation of agar phantoms containing AuNPs concentrated in a small well with a NIR laser, in similarity of what was previously reported (Ferreira-Gonçalves et al., 2022). Briefly, agar phantoms were prepared starting with the aqueous dissolution of agar (1 %, *w/v*) under magnetic agitation and heating until water ebullition (100 °C). Then, 1 mL of such solution was poured into polystyrene cuvettes. After gelation of the agar solution at 2 °C, small wells were made in the center of the agar and 20 μL of each AuNPs solution to test were added to the wells of testing phantoms. In addition, positive control phantoms were prepared by incorporation of small black plasticine spheres (diameter of 0.40 ± 0.05 cm) in the wells, and negative controls were prepared by leaving the wells empty and further filling them with agar. Next, one more milliliter of agar solution was added to each phantom, in order to completely fill the wells and approximately place the AuNPs solutions in the center of the phantoms. Once the phantoms were prepared, they were assembled in the experimental setup previously reported (Ferreira-Gonçalves et al., 2022). A thermocouple (Fluke 52 K/J thermometer, Everett, WA, USA) was added to the phantoms to measure the temperature of the agar surrounding the wells before, during and after irradiation with a FC-808–2 W Fiber Coupled Laser System (Frankfurt Laser Company, Friedrichsdorf, Hessen Germany) coupled to a FPYL-COL-X collimator (Frankfurt Laser Company, Friedrichsdorf, Hessen Germany) emitting at a wavelength of 808 nm (within the NIR range). For irradiation, the laser beam was centered and aligned to irradiate the testing samples. The irradiation was maintained up until 10 min and an irradiance of 7.96 W/cm^2 was applied.

2.2.5. Photothermal conversion efficiency studies

It was important to have knowledge on the photothermal conversion efficiency of the produced AuNPs. Roper and co-workers firstly reported in 2007 (Roper et al., 2007) a collective heating model widely adapted to study the temperature profile of AuNPs once irradiated with a light beam (Ayala-Orozco et al., 2014; Jiang et al., 2013; Pu et al., 2018). Such studies, allow the determination of the AuNPs photothermal conversion efficiency (η) based on the energy balance of the system, which can be described as:

$$\sum_i m_i c_i \bullet \frac{dT}{dt} = Q_{AuNPs} + Q_{Dis} - Q_{ext} \qquad (W) \tag{8}$$

where: m_i and c_i are the mass and specific heat capacity of each component from the system (in this case, AuNPs, polystyrene cuvette and water); T is the system temperature; t is the time; Q_{AuNPs} is the heat generated by the AuNPs upon irradiation with a light source; Q_{Dis} is the heat dissipated in consequence of the light absorption caused by the cuvette filled with water (water, as the solvent used in these experiments); and Q_{ext} is the external heat flux, the heat conducted away from the system by air. External heat flux can be described as:

$$Q_{ext} = hA(T - T_{amb}) \qquad (W) \tag{9}$$

with, h the heat transfer coefficient, A the surface area coefficient, and T_{amb} the temperature of the air surrounding the system. By its turn, Q_{AuNPs} can be calculated based on:

$$Q_{AuNPs} = P\left(1 - 10^{-A_\lambda}\right)\eta \qquad (W) \tag{10}$$

where P is the power of the light source applied, A_λ the AuNPs absorbance at such wavelength (λ), and η the photothermal conversion efficiency of the light incident on the AuNPs into thermal energy.

When the system reaches a maximum temperature (T_{max}), an equilibrium is attained, and the heat generated due to AuNPs and cuvette absorption of the light equals the heat losses by external heat flux:

$$Q_{AuNPs} + Q_{Dis} = Q_{ext} = hA(T_{max} - T_{amb}) \qquad (W) \tag{11}$$

Thus, at this point, the photothermal conversion efficiency (η) of the AuNPs can be expressed as:

$$\eta = \frac{hA(T_{max} - T_{amb}) - Q_{Dis}}{P\left(1 - 10^{-A_\lambda}\right)} \qquad (\%) \tag{12}$$

In order to assess η, 2 mL of aqueous solutions of Core AuNPs at a concentration of 125 μM of Au were transferred to polystyrene cuvettes and irradiated with a FC-808–2 W Fiber Coupled Laser System emitting at a wavelength of 808 nm (Frankfurt Laser Company, Friedrichsdorf, Hessen Germany) coupled to a FPYL-COL-X collimator (Frankfurt Laser Company, Friedrichsdorf, Hessen Germany). A power of 1.44 W was applied and the absorbance of the AuNPs at the irradiation wavelength have been previously assessed. The temperature of the solution was measured during heating (laser ON) and cooling (laser OFF) phases by immersing a thermocouple (Fluke 52 K/J thermometer, Everett, WA, USA) into the testing solutions, ensuring that the laser beam wouldn't directly irradiate the thermocouple. Attending the temperature measured over time a dimensionless driving force, θ, can be introduced and scaled using the maximum system temperature, to allow to find hA to input on the equation to determine η. The dimensionless driving force, θ, can be defined as:

$$\theta = \frac{T_{amb} - T}{T_{amb} - T_{max}} \tag{13}$$

Furthermore, an additional time constant, τ_s is introduced and described as:

$$\tau_s = \frac{\sum_i m_i c_i}{hA} \tag{14}$$

allowing later to find hA. When the laser is switched OFF, the system starts to cool down and the sum of the heat generated by AuNPs, and the heat generated by the cuvette filled with the solvent equals zero. Thus, by rearranging the previous equations it is found that:

$$\frac{d\theta}{dt} = -\frac{\theta}{\tau_s} \tag{15}$$

In addition, once the laser is switched OFF (t = 0 s), the temperature of the system corresponds to the maximum temperature (T_{max}), allowing to obtain τ_s from the slope of the plot of t as function of ln (θ):

$$t = \tau_s(-\ln(\theta)) \tag{16}$$

Hence, hA can be further calculated by:

$$hA = \frac{\sum_i m_i c_i}{\tau_s} \quad (17)$$

As previously referred, our system includes the polystyrene cuvette (the container), water (the solvent) and the AuNPs. According to the literature, the specific heat capacity of Au, water and polystyrene are 0.129 J $g^{-1}K^{-1}$ (Jiang et al., 2013; The Engineering ToolBox, 2003), 4.18 J $g^{-1}K^{-1}$ (Ayala-Orozco et al., 2014; Jiang et al., 2013; The Engineering ToolBox, 2003), and 1.4 J $g^{-1}K^{-1}$ (The Engineering ToolBox, 2003), respectively. As c_{Au} is much smaller than c_{H2O} and $c_{Polystyrene}$, the participation of the AuNPs will be neglectable in similarity to what was done by others (Roper et al., 2007). The value of Q_{Dis} was estimated using the methodology described before for a cuvette simply filled with water (with no AuNPs). In this case, once the laser is OFF, $Q_{Dis} = Q_{ext}$, and so, after finding hA and replacing it into Equation (11), Q_{Dis} can be found.

2.2.6. Preliminary in vivo safety assays using Artemia salina model

AuNPs' preliminary *in vivo* safety was assessed using *Artemia salina*, a widely used lethality assay to check the toxicity of materials like nanoparticles (Ferreira-Gonçalves et al., 2022; Rajabi et al., 2015). The methodology followed was published before (Ferreira-Gonçalves et al., 2022). Briefly, *Artemia salina* eggs were hatched in commercial sea water for 48 h, under aeration and continuous illumination, and at temperatures ranging from 25 to 30 °C. For incubation with the test solutions, 900 μL of artificial sea water containing 10–15 nauplii were transferred to each well of a 24-well plate. Next, 100 μL of each test solution was added to the wells: artificial sea water (as mortality negative control); AuNPs from both Cores at different Au concentrations (625 μM up to 5000 μM of Au in artificial sea water); and 100 % DMSO (as mortality positive control). The nauplii were left exposed to test solutions for 24 h under the same growth conditions, with exception to the aeration. The number of dead nauplii after 24 h of exposure to the test solutions ($Dead_{24h}$) was counted and 100 μL of 100 % of DMSO were added to each well to kill the remaining *artemia*. The total *artemia* per well was counted ($Dead_{Total}$) and the mortality (%) was determined as follows:

$$Mortality\ (\%) = \frac{Dead_{24h}}{Dead_{Total}} \times 100 \quad (18)$$

As a note, all samples were tested three times with 3 replicates each.

2.2.7. Preliminary in vivo safety of AuNPs using healthy mice

For this study healthy BALB/c female mice supplied by Charles River (Barcelona, Spain) were fed standard diet and water *ad libitum* and housed in polypropylene cages at ambient temperature (20–24 °C), relative humidity (55 ± 5 %) and 12 h light/dark cycle. All experiments involving animals were approved by the competent national authority (Direção Geral de Alimentação e Veterinária, DGAV), carried out in compliance with the 3R's principles, the accepted principles for laboratory animals, and in accordance with the Animal Welfare Organ (ORBEA) of the Faculty of Pharmacy, University of Lisbon. Moreover, national (DL 113/2013, 2880/2015, 260/2016 and 1/2019) and international (Directive 2010/63/EU) legislation including guidelines for the Care and Use of Laboratory Animals were respected.

The animals were randomly distributed into seven groups (n = 3, except for control, i.e., animals not receiving any AuNPs administration with n = 2): Control, and animals exposed to Core 1 and Core 2 AuNPs, both 4 h, 24 h and 48 h.

Prior AuNPs injection animals were shaved at the injection region using an electric shaver. The animals were daily weighted before and after injection of the AuNPs, and the animals' welfare was also monitored. All animals under study received a suspension of AuNPs at a dose of 3.1 mg/kg of body weight in terms of Au content (AuNPs suspended in PBS 1x, pH 7.4). The selected dose was based in previous work already published, from the group, reporting the administration of hyaluronic and oleic acids-coated AuNPs (HAOA-AuNPs) (Lopes et al., 2021). A subcutaneous injection of the AuNPs into the animals' right flank was chosen as it will be the local of administration of the AuNPs in the breast cancer model to be used in future efficacy studies. Such studies will be carried out in MCF-7-induced xenograft models, in which tumors will be grown in the animals flank, in similarity to what was reported by others (Ciccone et al., 2018; Zhang et al., 2020), and the AuNPs will be administered locally (intra tumor).

After injection of AuNPs, the animals returned to their housing and posteriorly were sacrificed at different time points. For the sacrifice, animals were anesthetized with inhalation of isoflurane and blood was collected for quantification of the Au that reached blood circulation. The injection site and some vital organs (liver, spleen, and kidneys) were also collected. The organs were primarily weighted to calculate the tissue indexes according with the following equation:

$$tissue\ index = \sqrt{\frac{organ\ weight}{body\ weight}} \times 100 \quad (19)$$

Subsequently, the organs were divided into two portions: one for histopathological analysis and one for ICP analysis to quantify Au content. For ICP analysis the tissues were firstly frozen and lyophilized. For histopathological analysis, tissue samples were fixed in 10 % buffered formalin, processed for routine Hematoxylin and Eosin staining (H&E staining) and examined using a conventional light Olympus CX21 microscope (Olympus Corporation, Tokyo, Japan).

2.2.8. Supportive evidence of local retention of AuNPs in in vivo models using CT scan

In addition to the aforementioned studies, other mice received once AuNPs (3.1 mg/kg of body weight, suspended in PBS 1x, pH 7.4) and were subjected to computerized tomography (CT) weekly up to 1-month post-injection to track the AuNPs at the site of administration. Prior the CT exam, the animals were anesthetized with a mixture of ketamine and medetomidine, and once the exam was over, anesthesia was reversed with atipamezole. For images acquisition a Toshiba Astelion 16 CT scanner (Toshiba, Tokyo, Japan) was used, applying the following scan parameters: 120 kV; 250 mA; rotation time of 0.75 s; 0.5 mm slice thickness; pitch factor of 0.688; and helical pitch of 11 with 16 rows. Later, the images were analyzed using RadiAnt DICOM Viewer (Version 2022.1.1 64-bit, Medixant, Poznan, Poland) as DICOM image processing software.

2.2.9. Preliminary in vitro efficacy using 2D culture of 4T1, MCF-7 and HaCaT cells

The photothermal efficacy of the combination of AuNPs with NIR laser irradiation was assessed in 2D culture models of commercial cell lines using the 3-(4,5-Dimethylthiazol-2-yl)-2,5-Diphenyltetrazolium Bromide (MTT) cell viability assay. The day before incubation of the particles, cells at a concentration of 5 x 10^4 cells/mL were seeded in 96-well plates. In this assay it was compared the effect of the AuNPs and laser irradiation alone with the synergistic effect of AuNPs and laser irradiation. Cells intended to receive laser irradiation (both alone or combined with AuNPs) were separated by one empty well in all directions in order to avoid collateral undesirable scattered or reflected light from adjacent wells. AuNPs were tested at a concentration of 250 μM of Au in culture medium and a period of 4 h of incubation was applied, based on previous incubation periods reported by our group (Silva et al., 2016a). After the 4 h incubation period, the medium with unbound AuNPs was substituted by 100 μL of fresh complete medium. Moreover, in order to subject all the cells to the same handling conditions, the medium from cells not treated with AuNPs was also replaced. The cells were then irradiated with the same laser system and using the same irradiance from the *in vitro* thermal activation studies using phantoms. The laser beam was centered and aligned with each well and the irradiation was maintained during 5 min.

Twenty-four hours after laser irradiation, the culture medium was removed and the cells washed twice with PBS (PBS 1x, pH 7.4). Then, 50 μL of a MTT solution at 0.5 mg/mL in incomplete medium were added to the cells and allowed to incubate for 4 h. Later, 200 μL of DMSO were added to each well in order to dissolve the formazan crystals produced by the cells upon MTT reduction. The absorbance was then read at 570 nm using a BioTek ELx800 Absorbance Microplate Reader (BioTek Instruments, Inc., Winooski, VT, USA) and the cells' viability (%) calculated as follows

$$Cell\ viability\ (\%) = \frac{OD_t}{OD_c} \times 100 \quad (20)$$

with OD_t being the optical density of the cells from testing groups and OD_c the optical density of control cells (cells only in culture medium corresponding to 100 % cell viability).

2.2.10. Statistical analysis

All data are represented as mean ± standard deviation (SD) for referred n. Statistical differences were considered when *p-value* < 0.05 and analyses were carried out in GraphPad Prism 8® (San Diego, California, USA). The main physicochemical properties of the four types of AuNPs were compared by applying a one-way ANOVA followed by Tukey's multiple comparisons test. The main features of the two core AuNPs prepared after scaling-up the syntheses were compared using the t-student test. One-way ANOVA followed by Tukey's multiple comparisons test was also applied to compare the mortality (%) of the two scaled-up Core AuNPs tested in *Artemia salina* model. AuNPs sizes determined by DLS and by SEM were compared using a two-way ANOVA followed by Sidak's multiple comparisons test. Differences on the photothermal activation properties were compared using a two-way ANOVA followed by Tukey's multiple comparisons test. Lastly, differences on the cells' viability caused by AuNPs and/or laser treatment in comparison to Control cells were assessed using a one-way ANOVA followed by Dunnett's multiple comparisons test.

3. Results and discussion

The global market of gold nanoparticles has been evaluated in more than 6600 million USD in 2022, and it is expected to continue growing (Research, 2023). Its compound annual growth rate is estimated to be 22.3 % from 2023 to 2030 (Research, 2023), which is greatly due to the increasing use of AuNPs in biomedical, pharmaceutical and dentistry fields. Despite the increasing attention and high number of publications on AuNPs' production methods and biomedical and pharmaceutical applications (Ortiz-Castillo et al., 2020), only a few cases have made it until clinical trials phase. To date (October, 2023), 37 clinical trials involving AuNP-based systems were found (https://clinicaltrials.gov/). Of those, 31 proposed the use of AuNPs as part of therapeutic systems and 6 as diagnostic tools. Among the AuNP-based therapeutic systems, 4 have been proposed for the treatment of inflammatory diseases (NCT05347602, NCT05268718, NCT02219074 and NCT02217228), 2 for vascular diseases (NCT01270139 and NCT01436123), 6 for infectious diseases (NCT05816512, NCT03669224, NCT05113862, NCT04935801, NCT05633446 and NCT06000514), 1 for metabolic diseases (NCT02837094), 11 for neurodegenerative diseases (NCT03815916, NCT03843710, NCT03993171, NCT04098406, NCT02755870, NCT03536559, NCT04081714, NCT04414345, NCT04297683, NCT04626921 and NCT05299658), and 7 for cancer (NCT03020017, NCT00356980, NCT00436410, NCT00848042, NCT01679470, NCT02680535 and NCT04240639). The gap between the academic research and the clinical translation of AuNP-based medicines is in part related with the unknown long term *in vivo* AuNP' toxicity and accumulation (Nguyen and Falagan-Lotsch, 2023; Zhang et al., 2023). Moreover, the complexity of formulations is also pointed out as one of the reasons slowing down their clinical translation, making it harder to scale up their production process (Zhang et al., 2023).

The use of AuNPs as part of PTT systems is not a new proposal. It is rather a commonly explored field in constant growth due to the high potential it presents. In fact, AuNPs were already used in 7 clinical trials involving PTT (NCT01270139, NCT01436123, NCT05268718, NCT00848042, NCT01679470, NCT02680535 and NCT04240639). There is still a broad range of challenges to address and improve until AuNPs can represent a viable option available in the clinic. Anisotropic AuNPs are often pointed out as one of the most promising types of AuNPs for PTT, as they present excellent optical and catalytical properties (Arellano et al., 2023; Ortiz-Castillo et al., 2020; Zhang et al., 2023). However, these particles are also associated to some concerns, namely production reproducibility and the use of certain toxic reagents (Li et al., 2014). In addition, Wang *et al.* reported a lower toxicity of spherical AuNPs of different sizes in human skin cells than gold nanorods (Wang et al., 2008), which was associated to the presence of CTAB on the nanorods' coating. The use of toxic reagents and stabilizers for the production of AuNPs have been more frequently replaced by more environmentally friendly and biocompatible alternatives (Ferreira-Gonçalves et al., 2021; Sengani et al., 2017; Sztandera et al., 2019). Nevertheless, those alternatives are often associated to AuNPs homogeneity concerns (Ortiz-Castillo et al., 2020; Shankar et al., 2004), which hinders further biomedical and pharmaceutical applications as it makes it harder to assess and predict the AuNPs' toxicity and biological behavior. Thus, herein it was proposed an adaptation of a recently reported bio-based synthetic method by our group, in order to explore a simpler, more reproducible, and scalable production of AuNPs aimed to be used as part of a PTT system.

3.1. Characterization of AuNPs from small-volume batches

3.1.1. Physicochemical characterization of AuNPs from small-volume batches

In similarity and continuation of the work previously published (Ferreira-Gonçalves et al., 2022), AuNPs obtained upon variation of the $HAuCl_4 \cdot 3H_2O$ concentration used on their synthesis were physicochemically characterized using DLS, electrophoretic mobility and spectroscopy analysis. In a primary macroscopical analysis it was noticed a clear difference between the AuNPs suspensions obtained based on their colors (Figure S1, which can be found as supplementary data in Appendix A): Core 1 AuNPs presented a red-brownish color; Core 2 AuNPs a blue-greyish color; Core 3 AuNPs a burgundy color; and Core 4 AuNPs a light-pink color.

Further physicochemical characterization of the obtained AuNPs is shown in Table 2. DLS size frequency distribution graphs can further be found in Figure S2 from the supplementary material in Appendix A. Attending the AuNPs size, Core 3 AuNPs seemed to be the smallest and Core 2 AuNPs the largest. No tendency between the Au salt concentration and the size of the obtained AuNPs was, however, noticed. Moreover, Core 4 AuNPs presented a wide variation in terms of size, which hindered the perception of any tendency. As for the polydispersity of AuNPs, Core 2 and Core 4 AuNPs presented lower polydispersity, when comparing with the other two cores. Yet, just like in terms of size, no tendency between the Au salt concentration and the PdI value was observed. In a first analysis, size and PdI results from Core 4 AuNPs seem contradictory, as they present the highest size variation and the lowest PdI average value. Nonetheless, it must be noticed that despite both parameters represent average values from different batches, the wide variation in size represents a higher variability between batches, whereas the PdI represents the formulation homogeneity within batch. Thus, the size and PdI values observed for Core 4 AuNPs unveil limited synthesis reproducibility, even though the synthesis homogeneity is good. Similar values of surface charge were observed for all the AuNPs, however, Core 4 AuNPs presented more positive surface charges than the other AuNPs. Moreover, it might seem that by reducing the Au salt concentration the surface charge was increased. Considering then the

Table 2
Physicochemical characterization of AuNPs at syntheses concentration depending on the Au salt content used for the syntheses.

	Core 1 AuNPs	Core 2 AuNPs	Core 3 AuNPs	Core 4 AuNPs
Hydrodynamic Diameter (nm)	97.4 ± 21.9	146.0 ± 20.0**	42.2 ± 2.3$^{**,\#\#\#\#}$	90.5 ± 42.0$^{\#\#}$
PdI	0.355 ± 0.103	0.148 ± 0.048***	0.388 ± 0.032$^{\#\#\#}$	0.158 ± 0.049$^{**,++}$
Zeta-Potential (mV)	−23.5 ± 7.0	−24.9 ± 3.2	−20.5 ± 1.8	−12.8 ± 1.5$^{*,\#\#}$
Maximum Absorbance Peak (nm)	601 ± 42	666 ± 42*	540 ± 3$^{\#\#\#}$	526 ± 2$^{\#\#\#}$
Absorbance at 808 nm[1] (a.u.)	0.68 ± 0.04	0.69 ± 0.05	0.05 ± 0.01$^{****,\#\#\#\#}$	0.02 ± 0.01$^{****,\#\#\#\#}$

For spectroscopy and DLS analyses, AuNPs were suspended in Milli-Q water. For electrophoretic mobility analyses, AuNPs were suspended in PBS 1× (pH 7.4, USP32). [1] Solution at syntheses concentration with no uniformization in terms of Au content. Data represented as mean ± SD, n > 3. Statistical significance is represented as * $p < 0.05$, ** $p < 0.01$, *** $p < 0.001$ and **** $p < 0.0001$ comparing with Core 1 AuNPs; ## $p < 0.01$, ### $p < 0.001$ and #### $p < 0.0001$ comparing with Core 2 AuNPs; ++ $p < 0.01$ comparing with Core 3 AuNPs.

absorbance spectra of the different AuNPs (Fig. 1), it is clear that when Au salt concentration was reduced, the spectra presented a narrower maximum absorbance peak with low intensity (<0.5 a.u.) within the visible range (≈ 530 nm). Furthermore, both Cores 3 and 4 AuNPs showed very low absorbance within the NIR range. By its turn, Core 1 AuNPs despite presenting a characteristic spectrum (relatively narrow peak of maximum absorbance within the visible range), exhibited variable maximum absorbance peaks. Nevertheless, the absorbance of the AuNPs within the NIR range was still high (>0.5 a.u.). Lastly, Core 2 AuNPs presented a distinct spectrum with a broader absorbance band centered within the NIR range. In similarity with Core 1 AuNPs, Core 2 AuNPs also presented high absorbance (>0.5 a.u.) through all NIR range, nevertheless, when approaching far NIR range (λ > 900 nm), Core 1 AuNPs showed enhanced absorbance than Core 2 AuNPs. As a note, the here so called "Core 1 AuNPs" were already described in a previously published work (AuNPs called "Ratio 3 AuNPs") (Ferreira-Gonçalves et al., 2022) and the characterization herein shown agrees with what was previously reported, which shows the AuNPs syntheses reproducibility.

The main goal of the presented work was to obtain AuNPs with high potential to be used as part of a PTT system combining *in situ* injection of AuNPs with laser irradiation (within the NIR range, 780 – 3000 nm, defined in accordance with ISO 20473:2007 Optics and photonics - Spectral bands). Thus, considering the future application intended for the AuNPs, it was possible to triage the AuNPs prepared.

As a start point of decision, thinking on the intended type of administration, size is a relevant feature to consider. For the envisioned application, AuNPs are needed to be retained at the injection site, minimizing their migration to non-target tissues, and retarding their removal by elements from the immune system. According with the literature (Schleh et al., 2012; Sonavane et al., 2008), larger AuNPs (>200 nm) present more difficulties to widely distribute, as well as to cross barriers such as the haemato-intestinal and the skin, than smaller AuNPs. In contrast, small AuNPs (<20 nm) can not only widely diffuse throughout the body, as they already proved to be able to cross both placenta and blood–brain barriers (Hillyer and Albrecht, 2001; Schleh et al., 2012; Semmler-Behnke et al., 2014). Thus, AuNPs with sizes around 200 nm seem to be preferential to achieve the goals proposed (Van Haute and Berlin, 2017). With this in mind, Core 2 AuNPs seem to be the most adequate.

Surface charge is other parameter influencing the AuNPs behavior *in vivo*. Positively charged nanoparticles are associated to higher toxicity and poorer stability than their negatively charged counterparts (Fröhlich, 2012; Lin et al., 2010). Moreover, negatively charged nanoparticles already showed enhanced accumulation at tumors (Honary and Zahir, 2013). Thus, negatively charged AuNPs are preferable over positively charged ones for the intended application. As all AuNPs obtained presented negative surface charge, surface charge cannot act as decision factor.

Another parameter possible to use as decisive factor is PdI. Polydispersity index is suggestive of the nanoparticle's homogeneity and, according to the ISO 22412:2017, 2017, a PdI < 0.7 is indicative of a monodisperse population of spherical particles. Other sources state that samples with PdI < 0.4 are considered to be homogeneous (Eissa, 2019). This limit can even be lower (<0.3) (Danaei et al., 2018). Thus, attending the values herein observed, all prepared AuNPs were homogeneous, with Core 2 and Core 4 AuNPs seeming to be more homogeneous than the remaining AuNPs.

At last, another crucial factor for selecting the most promising formulation for the intended application is the AuNPs' absorbance. As mentioned above, the proposed system relies on the combination of AuNPs injection with external irradiation with a NIR laser (λ = 808 nm), which emphasizes the need of the AuNPs to absorb as much as possible at wavelengths close to the wavelength of the light source used. Thus, Core 2 AuNPs were the most promising followed by Core 1 AuNPs, not only because they presented maximum absorbance peaks at longer wavelengths (approximately at 665 nm and 600 nm, respectively), but also because they showed higher absorbance at the laser wavelength. As aforementioned, the laser wavelength was selected within the NIR range as it is known as a spectral region where biological tissues present lower

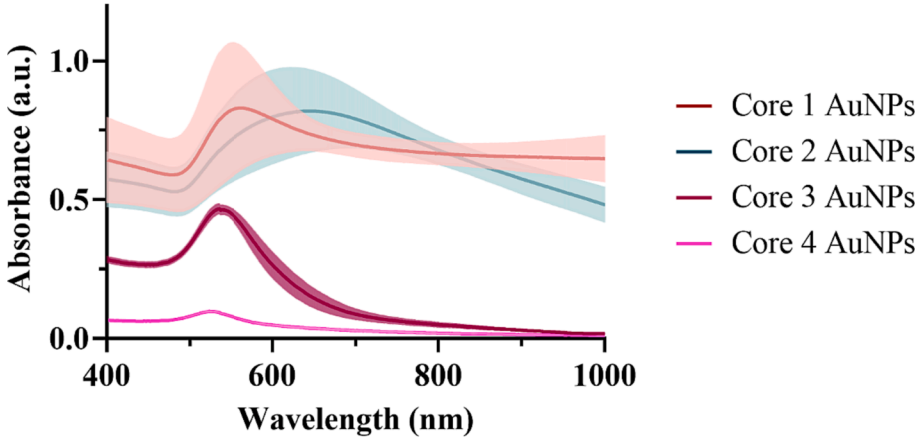

Fig. 1. Absorption spectra of different AuNPs' suspensions. Data represented as mean ± SD, n > 3.

absorbance of the radiation, and thus makes possible to reach deeper tissues (Bashkatov et al., 2005; Jacques, 2013).

3.1.2. Morphological characterization of AuNPs from small-volume batches

The morphological aspect of the four types of Core AuNPs was observed by SEM and it is shown in Fig. 2. All Core AuNPs showed a predominant spherical-like shape, however, there were clear morphological differences between Core AuNPs. Core 1 and Core 2 AuNPs both presented significative surface roughness, in contrast with Core 3 and Core 4 AuNPs, which showed very smooth surfaces. When comparing Core 1 AuNPs and Core 2 AuNPs in terms of surface roughness, Core 1 AuNPs revealed accentuated roughness with edgy contours, whereas Core 2 AuNPs showed high roughness with softer contours instead. Nanoparticles' surface roughness is known to affect the protein corona formation and, consequently, to affect the particles' internalization (Kim et al., 2021; Singh et al., 2021). Some studies report that higher surface roughness leds to enhanced protein adsorption in comparison with smoother surfaces (Rechendorff et al., 2006; Singh et al., 2018). Moreover, studies also showed that silica-based nanoparticles with smooth surfaces present faster and more pronounced internalization in HeLa cells than rougher counterparts (Schrade et al., 2012). In addition, protein-coated smooth nanoparticles also showed higher cellular uptake than rougher counterparts (Piloni et al., 2019). Yet, there are also works showing that rougher nanoparticles present lower protein absorption than smother particles (Piloni et al., 2019). Thus, despite recognized the importance of the surface roughness of a material in pharmaceutical and biomedical applications, its effect over protein absorption and cellular uptake is still not consensual and requires further studies (Piloni et al., 2019). Nonetheless, in this work the prepared AuNPs vary more than one property between Cores, which hinders to acknowledge the isolated role of the surface roughness on the overall photothermal and biological behavior.

Attending AuNPs size, Core 2, Core 3, and Core 4 AuNPs present sizes slightly smaller (110.4 ± 20.9 nm, 31.5 ± 5.6 nm and 21.6 ± 5.8 nm, respectively) than the ones observed by DLS, which agrees with the literature (Bootz et al., 2004). In contrast, Core 1 AuNPs appeared much larger (362.0 ± 44.8 nm) by SEM than by DLS ($p > 0.0001$). Once this considerable size-difference was not observed for no other particles and that it is not typically described in the literature, it is hypothesized that it might be a consequence of the edgy roughness of the Core 1 AuNPs surface.

Based on the overall physicochemical features and the very low absorbance within the NIR range, Core 3 and Core 4 AuNPs were at this point abandoned, and further scaled up syntheses and a more thorough characterization was carried out for Core 1 and Core 2 AuNPs.

3.2. Comprehensive characterization of AuNPs from scaled-up syntheses

3.2.1. Physicochemical characterization of AuNPs from scaled-up syntheses

A summary of the main features of the prepared AuNPs after scaling up the syntheses from 20 mL to 100 mL is shown in Table 3. As complement, DLS size frequency distribution graphs can further be found in Figure S3 from the supplementary material in Appendix A. Comparing with smaller volume syntheses, Core 1 AuNPs presented overall similar physicochemical properties, even though it was noticed lower variation on the physicochemical parameters accessed (lower SD). Furthermore, a significant difference ($p < 0.01$) was seen over Core 1 AuNPs spectra from bigger syntheses, being a narrower maximum absorbance peak observed around 560 nm in contrast with the more variable peak centered around 601 nm observed for lower volume syntheses (Figs. 1 and 3). By its turn, Core 2 AuNPs from larger syntheses slightly differed from small volume syntheses counterparts in terms of size and spectra.

Table 3
Physicochemical characterization of Core 1 and Core 2 AuNPs resulting from scaled-up syntheses.

	Core 1 AuNPs	Core 2 AuNPs
Hydrodynamic Diameter (nm)	111.3 ± 27.7	192.1 ± 57.4
PdI	0.272 ± 0.080	0.223 ± 0.064
Zeta-Potential (mV)	−29.0 ± 2.0	−25.8 ± 2.1
Maximum Absorbance Peak (nm)	561 ± 17	751 ± 63**
Absorbance at λ = 808 nm[1] (a.u.)	0.14 ± 0.01	0.22 ± 0.05
Recovery yield (% (*n*/*n*))[2]	80 ± 8	98 ± 6**
Number of Au atoms per NP	(5.05 ± 3.91) x 10^7	(2.78 ± 2.24) x 10^8
Molar concentration of AuNPs[1] (M)	(3.69 ± 1.63) x 10^{-12}	(9.93 ± 9.30) x 10^{-13} *
Concentration of AuNPs[1] (AuNPs.mL^{-1})	(2.22 ± 0.98) x 10^9	(5.98 ± 5.60) x 10^8 *
Molar absorption coefficient at Max. absorption peak (M^{-1}.cm^{-1})	(7.08 ± 4.70) x 10^{10}	(4.25 ± 2.36) x 10^{11} *
Molar absorption coefficient at λ = 808 nm (M^{-1}.cm^{-1})	(5.41 ± 4.11) x 10^{10}	(4.11 ± 2.50) x 10^{11}

For spectroscopy and DLS analyses, AuNPs were suspended in Milli-Q water. For electrophoretic mobility analyses, AuNPs were suspended in PBS 1× (pH 7.4, USP32). Data represented as mean ± SD, with n > 3. Statistical significance is represented as * $p < 0.05$ and ** $p < 0.01$ comparing with Core 1 AuNPs. [1] Solution at the same Au concentration: 125 μM. [2] Quantification considering only the Au element based on ICP-OES analysis.

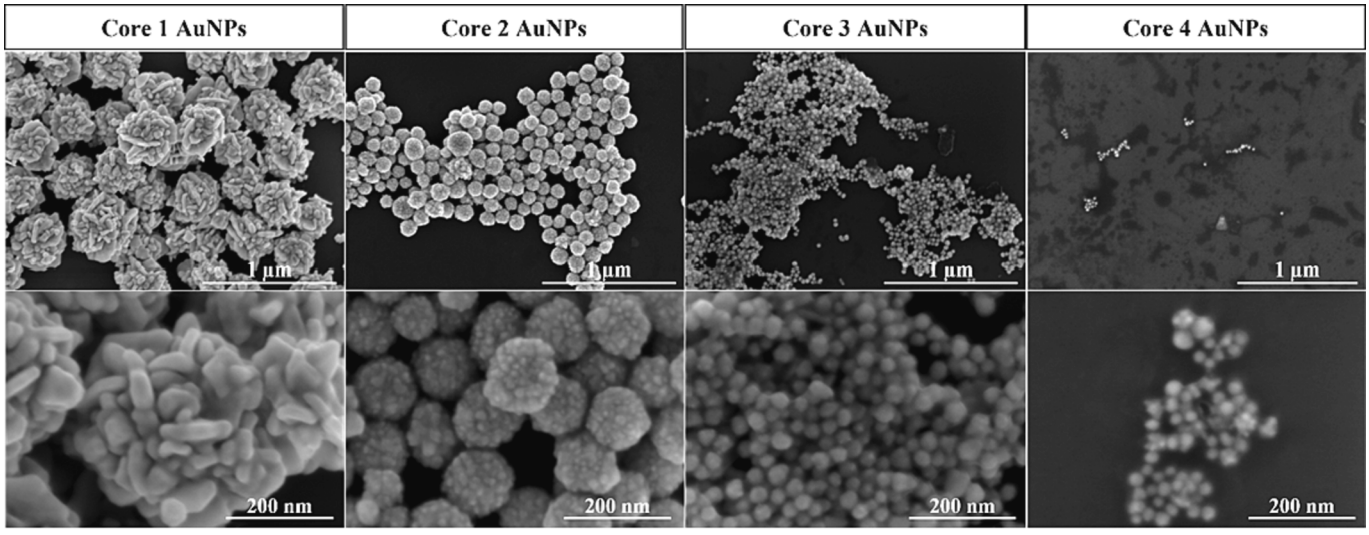

Fig. 2. Morphological characterization of Core 1, Core 2, Core 3 and Core 4 AuNPs by SEM.

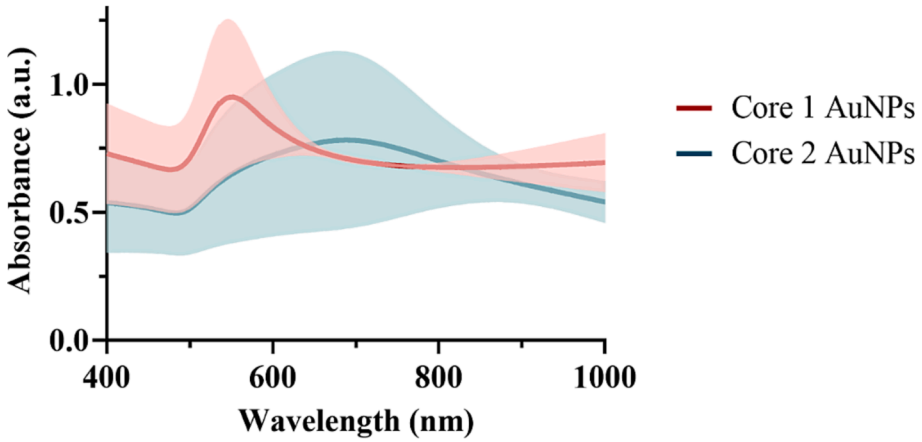

Fig. 3. Absorption spectra of different AuNPs' suspensions after scale up. Data represented as mean ± SD, n > 3.

Core 2 AuNPs from 100 mL syntheses were slightly larger ($p < 0.001$) than Core 2 AuNPs from 20 mL syntheses. Moreover, the spectra of Core 2 AuNPs from larger syntheses also presented a broader absorption band with maximum absorbance peak shifted towards the NIR range ($p < 0.0001$) than their counterparts from lower volume syntheses (Figs. 1 and 3). Regardless, the main differences on the physicochemical features between Core 1 and Core 2 AuNPs were retained: Core 2 AuNPs were larger and presented a broader absorbance band with maximum absorbance peak at longer wavelength than Core 1 AuNPs (Fig. 3). Attending then the additional characterization of the AuNPs carried out, Core 2 AuNPs presented a much superior recovery yield than Core 1 AuNPs. In addition, it was also found that Core 2 AuNPs had more atoms of Au per AuNP and, consequently, had less AuNPs per milliliter than Core 1 AuNPs for an equal concentration of Au. Moreover, Core 2 AuNPs presented higher molar absorption coefficient, both at the maximum absorbance peak and at $\lambda = 808$ nm, than Core 1 AuNPs, which means that lower concentrations of Core 2 AuNPs are needed to absorb the same amount of radiation. Thus, overall, Core 2 AuNPs presented more promising features to be better photothermal therapy enhancers.

The stability of the particles is also a major concern when aiming for biomedical and pharmaceutical applications. Thus, basic characterization of AuNPs was repeated 11 months after their synthesis upon being stored at 4 °C in aqueous suspension in glass flasks. Results are shown in Table 4 and Fig. 4. As observed, no significative changes were noticeable, thus demonstrating the AuNPs stability in the storage conditions.

Table 4
Physicochemical characterization of Core 1 and Core 2 AuNPs resulting from scaled-up syntheses, at the date of synthesis and 11 months later, upon storage at 4 °C in aqueous suspension.

	Core 1 AuNPs		Core 2 AuNPs	
	At synthesis	11 months after synthesis	At synthesis	11 months after synthesis
Hydrodynamic Diameter (nm)	96.4 ± 9.4	102.8 ± 16.1	195.7 ± 80.8	186.3 ± 73.8
PdI	0.287 ± 0.087	0.273 ± 0.086	0.221 ± 0.087	0.198 ± 0.091
Zeta-Potential (mV)	− 29.2 ± 2.1	−30.1 ± 1.2	−26.7 ± 2.3	−28.8 ± 2.0
Maximum Absorbance Peak (nm)	564 ± 18	565 ± 20	727 ± 50	735 ± 5

For spectroscopy and DLS analyses, AuNPs were suspended in Milli-Q water. For electrophoretic mobility analyses, AuNPs were suspended in PBS 1× (pH 7.4, USP32). Data represented as mean ± SD, with n > 2.

3.2.2. *Morphological characterization of AuNPs from scaled-up syntheses*

The morphology of Core 1 and Core 2 AuNPs obtained after scaling up the syntheses was also assessed by SEM (Fig. 5) and the main morphological features observed for AuNPs from small-volume syntheses were retained.

In addition to the AuNPs' morphology, the elemental constitution of the particles was assessed by combined SEM-EDS analysis (Fig. 6). Results showed gold as the most abundant element on the AuNPs (in green), without any other impurities present.

Core 2 AuNPs were also investigated using STEM analysis. As observed from the SEM images, it is evident that the AuNPs are nearly spherical and reveal a hierarchical rough surface, forming a peak-like structure (Fig. 7 (a) to (f)). Moreover, from the atomic resolution BF-STEM and HAADF-STEM images (Fig. 7 (g) and (h)), it is clear the atomic columns, where the visible spots correspond to Au atoms. The lattice fringe spacing marked with 0.235 nm corresponds to the {1 1 1} lattice planes of face-centered cubic (FCC) structure of Au. The inset presented in Fig. 7 (h) represents the Fast Fourier Transformation (FFT) image carried out in the area considered within the white squares in Fig. 7 (g) and (h), images obtained simultaneously. Observed through the $[10\bar{1}]$ zone axis, it is evident from the FFT pattern that the angle between (1 1 1) and $(\bar{1}1\bar{1})$ is ~ 109°, in accordance with the theoretical value reported for FCC-Au (JCPDS No. 65–2870).

3.2.3. *In vitro thermal activation studies using phantom models*

Thermal activation of AuNPs in a concentration-dependent way was studied by incorporation of AuNPs into agar phantoms and measuring the agar temperature increment over time upon irradiation with a NIR laser using a constant power. Results are shown in Fig. 8. In order to discard the effect of room temperature fluctuations over the results, only agar phantoms were analyzed without any irradiation and no significant temperature fluctuations were observed. Moreover, the influence of the laser irradiation over the thermocouple through direct heating of its material, was assessed by irradiating agar phantoms. No significant temperature increase was observed (maximum increment of 3.2 °C after 10 min of irradiation). A sphere of black plasticine was used as positive control of heating once it works as a strong absorber and thus potentiates a high temperature rise. Typical photothermal heating curves were observed, showing a faster temperature increase at initial times followed by an approximation to a stationary-like temperature increment state (Alrahili et al., 2020; Ferreira-Gonçalves et al., 2022). Overall, Core 2 AuNPs led to higher temperature increments for similar irradiation times at the same concentration than Core 1 AuNPs, nevertheless no significant statistical differences ($p < 0.05$) were observed between formulations regardless the concentration. Moreover, when at a gold concentration of 500 μM, Core 2 AuNPs presented an average temperature increment even higher than the one observed for the plasticine,

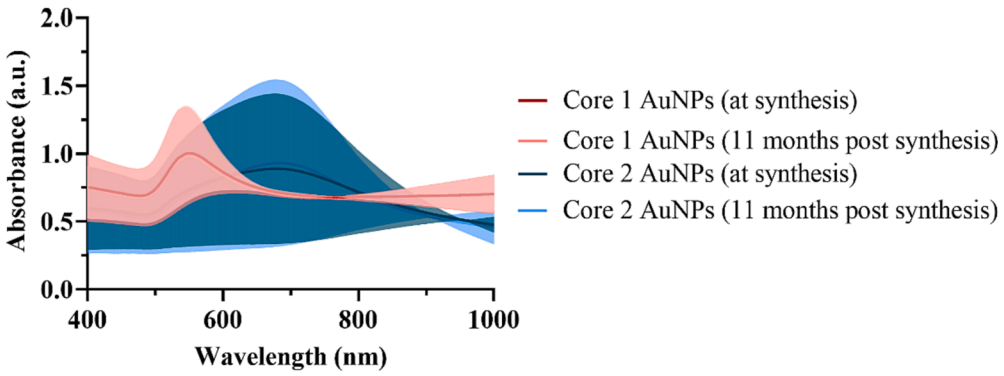

Fig. 4. Comparative absorption spectra of different AuNPs' suspensions after scale up, immediately after synthesis and up to 11 months later, upon storage at 4 °C in aqueous suspension. Data represented as mean ± SD, n > 3.

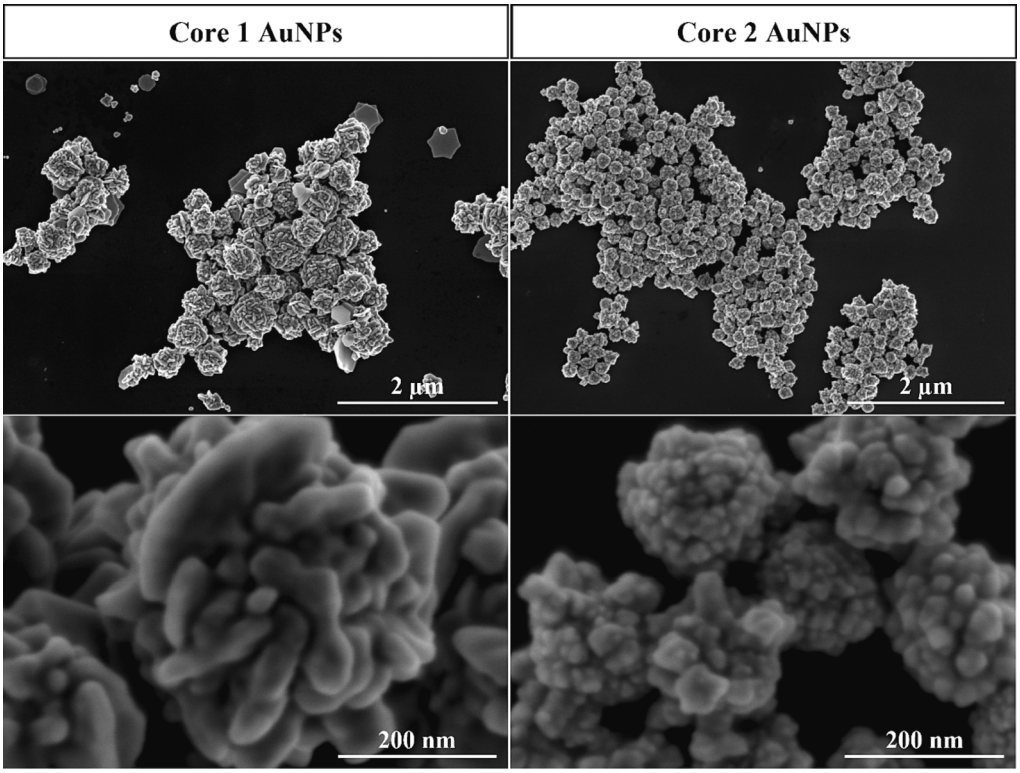

Fig. 5. Morphological characterization of Core 1 and Core 2 AuNPs after scale up by SEM.

which was not observed for Core 1 AuNPs.

Concerning the concentration-dependence, higher concentrations led to higher temperature increments, even though not all concentrations resulted in significant variations ($p < 0.05$). Regardless the concentration and type of AuNPs, no significant temperature increments were seen between 3 min and 5 min of irradiation, except for the case of Core 2 AuNPs at 500 μM of gold and the plasticine, in which after 5 min of irradiation the temperature increment was significantly higher than the one seen after 3 min of irradiation ($p < 0.05$). Core 1 AuNPs presented significant temperature increments after 10 min of irradiation in comparison with 3 min of irradiation for gold concentrations superior to 125 μM. Moreover, when Core 1 AuNPs were tested at gold concentrations higher than 250 μM, the temperature increments observed after 10 min of irradiation were even higher than the ones observed after 5 min of irradiation. By its turn, Core 2 AuNPs, regardless the gold concentration, showed significant increases of temperature after 10 min of irradiation when compared to the increments observed after 3 min and 5 min of irradiation ($p < 0.05$). Moreover, Core 2 AuNPs at 500 μM, after 5 min of irradiation already have heated up significantly more than after 3 min of irradiation ($p < 0.05$). Such observations were also seen for the plasticine.

According with the literature, humans' average basal temperature is around 37 °C (Geneva et al., 2019), and cell hyperthermia typically happens at approximate temperatures ranging from 41 °C up to 47 °C (Huang et al., 2008; Kumari et al., 2021). Thus, in order to have an enhanced PTT efficacy, temperature increments from 4 °C up to 10 °C are needed. Overall, Core 2 AuNPs allowed to reach higher temperature increments at lower concentrations and shorter irradiation periods. As a consequence, Core 2 AuNPs presented enhanced potential to be used in PTT system in comparison to Core 1 AuNPs, as they make it possible to use lower Au concentrations. Moreover, the fact that Core 2 AuNPs required shorter irradiation periods to reach higher temperature increments render the expectation for future *in vivo* applications.

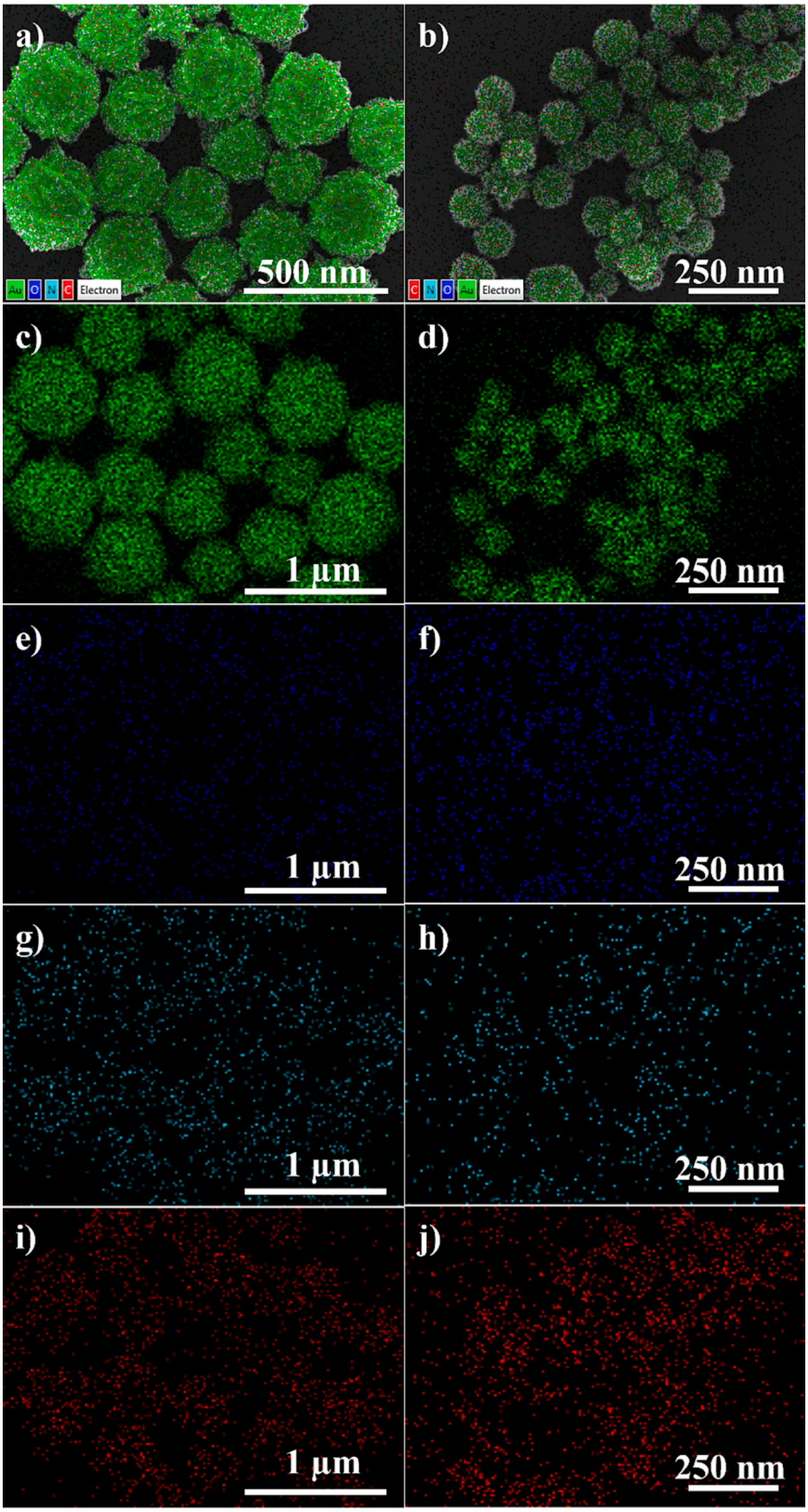

Fig. 6. Elemental characterization of Core 1 (**a**, **c**, **e**, **g i**) and Core 2 (**b, d, f**, **h**, **j**) AuNPs by EDS. (**a**) and (**b**) represent merged images of individual element identification images: (**c**) and (**d**) gold; (**e**) and (**f**) oxygen; (**g**) and (**h**) nitrogen; (**i**) and (**j**) carbon.

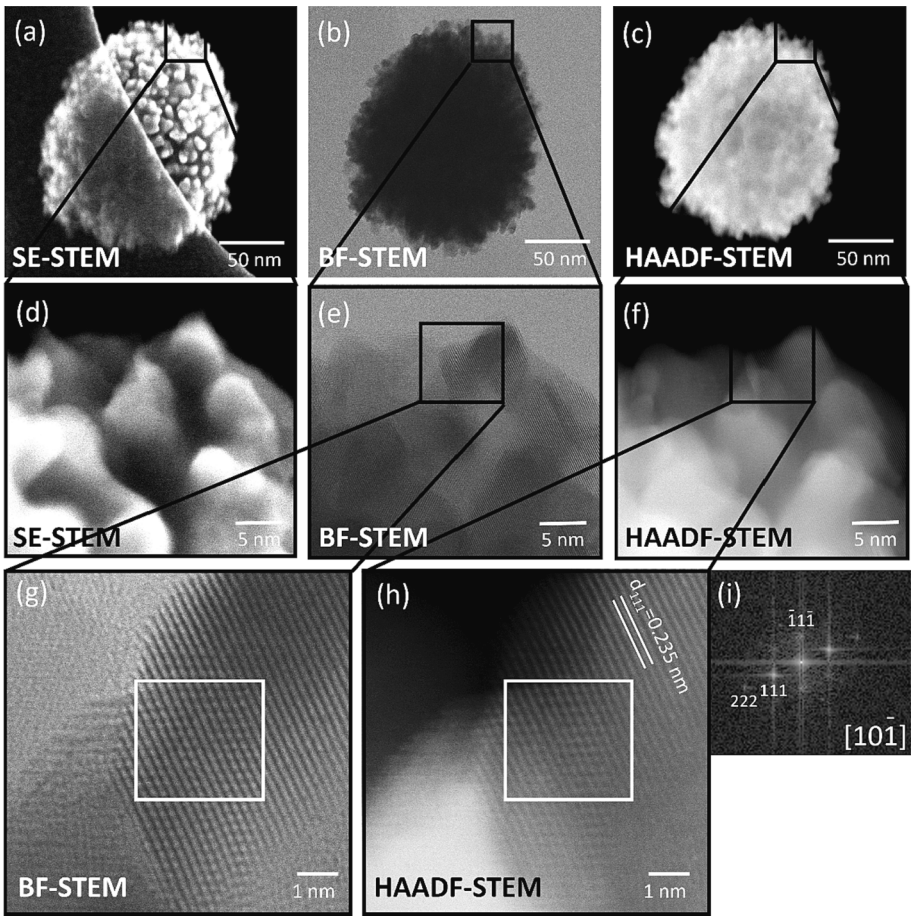

Fig. 7. (**a**) Secondary electron (SE) STEM image of an individual Core 2 AuNP, (**b**) Bright-field (BF) STEM image of the same area of (**a**), and (**c**) HAADF-STEM image of the area in (**a**) (images obtained simultaneously). (**d**) to (**f**) Magnified SE-STEM, BF-STEM and HAADF-STEM images of the area analyzed in (**a**), respectively. (**g**) Atomic-resolution BF-STEM and (**h**) HAADF-STEM images of the AuNP. (**i**) FFT image of the area indicated by the white squares in (g) and (h).

3.2.4. Photothermal conversion efficiency studies

The photothermal conversion efficiency of the AuNPs was determined upon direct irradiation of AuNPs aqueous suspensions with a NIR laser and direct measure of the solution temperature during and after irradiation, during heating and cooling phases, respectively. To minimize the interference of convection phenomena on the obtained results, the solutions were kept under mechanical stirring. Moreover, to minimize the temperature dissipation through air, the cuvettes containing the solutions were covered with parafilm. When at the same concentration and using the exact same irradiation parameters and setup, Core 2 AuNPs present a photothermal conversion efficiency of ≈ 58 % (Fig. 9), which is significantly higher than the ≈ 37 % observed for Core 1 AuNPs ($p < 0.05$). Even though, higher photothermal conversion efficiency not always means generation of more heat (Qin et al., 2016; Yang et al., 2021), this was the case for the tested AuNPs, as Core 2 AuNPs revealed a temperature increase of 19.7 ± 4.8 °C after 20 min of irradiation, in contrast with 7.0 ± 2.0 °C observed for Core 1 AuNPs.

The photothermal conversion efficiency of Core 1 and Core 2 AuNPs, in particular Core 2 AuNPs, are quite interesting when comparing with data from the literature as these values are among some of the higher already reported (Nardine S Abadeer and Murphy, 2016; Malekzadeh et al., 2023). Core 2 AuNPs showed higher photothermal conversion efficiency than ≈ 150 nm-sized gold nanoshells irradiated with a laser with comparable wavelength, having Pattani *et al.* reported 25 % photothermal conversion efficiency (Pattani and Tunnell, 2012) and Ayala-Orozco *et al.* 39 % (Ayala-Orozco et al., 2014). In addition, when compared with biodegradable gold vesicles (BGV) ≈ 200 nm-sized reported by Huang *et al.*, Core 2 AuNPs also showed superior photothermal conversion efficiency for the same wavelength radiation (≈ 58 % for Core 2 AuNPs compared with ≈ 37 % for BGV) (Huang et al., 2013). Moreover, Xu *et al.*, reported a photothermal conversion efficiency of ≈ 42 % for gold nanocages coated with hyaluronic acid with ≈ 190 nm irradiated with a 808 nm laser (X. Xu et al., 2019), which is also lower than the value herein observed for Core 2 AuNPs. It must however be noticed that this parameter strongly depends on the AuNPs features (such as size and shape), on their concentration, and on the irradiation parameters (e.g. wavelength, exposure time and irradiance). Thus, it is difficult to rigorously compare the results herein reported with data from the literature.

3.2.5. Preliminary in vivo safety assays using artemia salina model

The safety of the AuNPs was primarily assessed in a concentration-dependent way using a simple and commonly used *in vivo* model for toxicity evaluations: *Artemia salina* (Figure S4 from supplementary material in Appendix A). For the concentration range studied none of the Core AuNPs showed any toxicity over the *artemia* model in contrast with what was observed in the case of 10 % DMSO, which showed high toxicity.

3.2.6. Preliminary in vivo safety of AuNPs using healthy mice

The weight of the animals was monitored since the day of injection of the AuNPs until the time of sacrifice. No statistically significant weight losses were observed over time for none of the test groups. Animals injected with Core 1 AuNPs showed a weight loss of 2.1 ± 1.1 % and 3.6 ± 0.9 %, 24 h and 48 h post-injection, respectively. By its turn, animals injected with Core 2 AuNPs showed a weight loss of 1.5 ± 2.0 % and 3.0

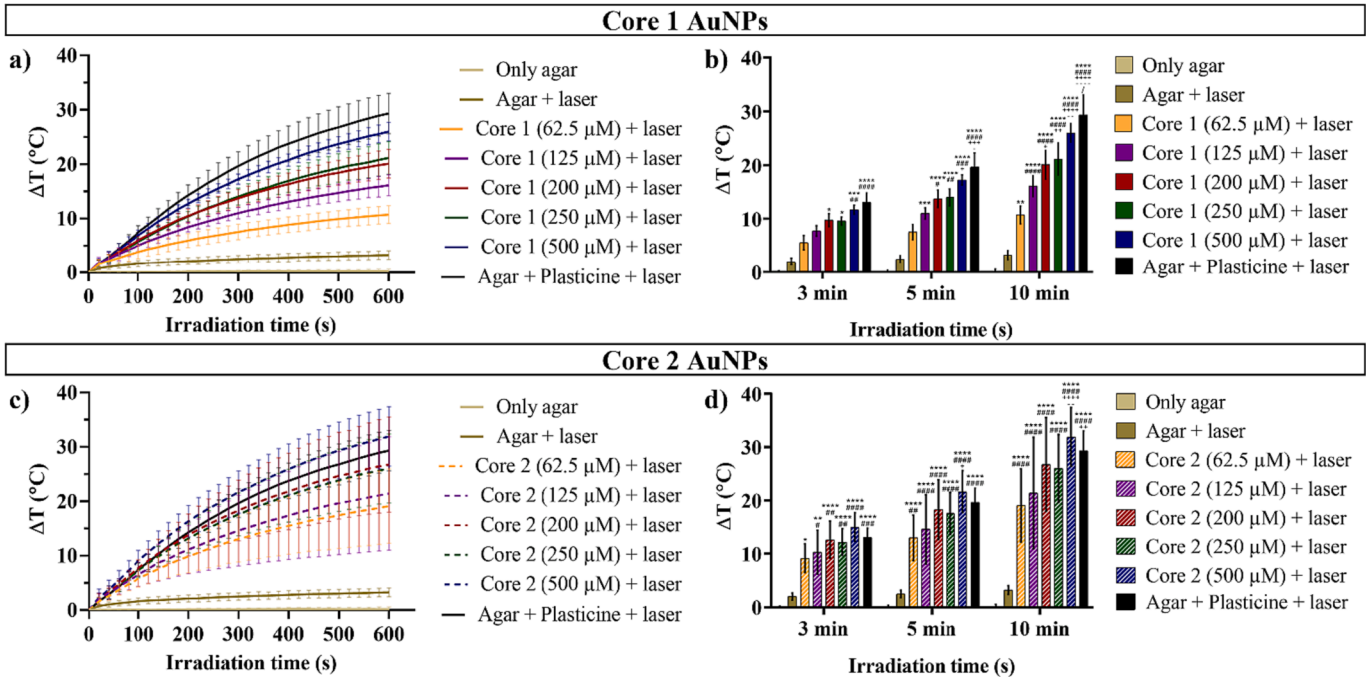

Fig. 8. Evolution of the temperature increment of phantoms containing Core 1 (a) and Core 2 (c) AuNPs and temperature increment after 3 min, 5 min and 10 min of irradiation of phantoms with Core 1 (b) and Core 2 (d) AuNPs. Tests carried out with AuNPs at different Au concentrations: 62.5 μM (orange), 125 μM (purple), 200 μM (red), 250 μM (green) and 500 μm (blue); and using as controls phantoms of only agar (beige), agar + laser (light brown) and agar + black plasticine + laser (black). Data represented as mean ± SD, n > 3. Statistical significance is represented as * $p < 0.05$, ** $p < 0.01$, *** $p < 0.001$ and **** $p < 0.0001$ comparing with only agar; # $p < 0.05$, ## $p < 0.01$, ### $p < 0.001$ and #### $p < 0.0001$ comparing with Agar + laser; + $p < 0.05$, ++ $p < 0.01$ and ++++ $p < 0.0001$ comparing with AuNPs at a concentration of 62.5 μM; - $p < 0.05$, - - $p < 0.01$ and - - - - $p < 0.0001$ comparing with AuNPs at a concentration of 125 μM; / $p < 0.05$ comparing with AuNPs at a concentration of 200 μM. (For interpretation of the references to color in this figure legend, the reader is referred to the web version of this article.)

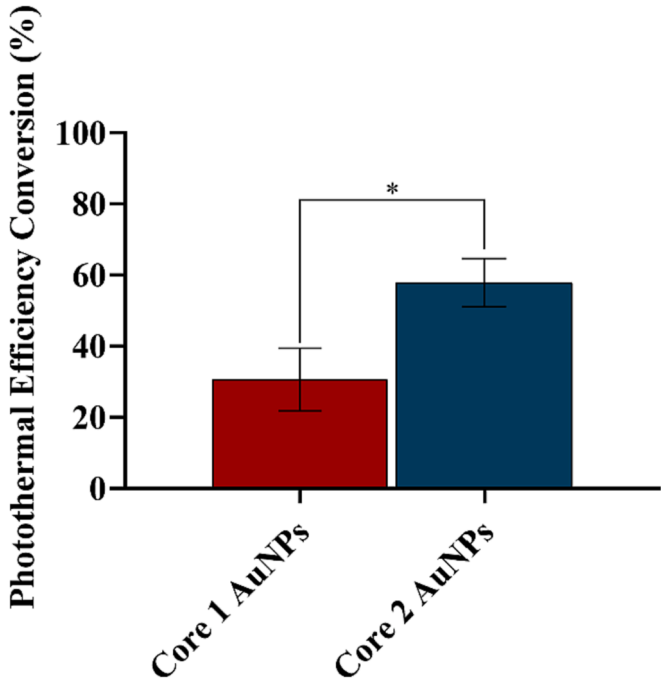

Fig. 9. Photothermal conversion efficiency of Core 1 and Core 2 AuNPs upon irradiation with a NIR laser (λ = 808 nm). Data represented as mean ± SD, n = 3. Statistical significance is represented as * $p < 0.05$ comparing with Core 1 AuNPs.

± 2.3 %, 24 h and 48 h post-injection, respectively.

At the end of the study, when excising the organs, no macroscopical abnormalities were observed in any organ for the animals under study. No further differences were either observed when analyzing the tissue index (%) of animals injected with AuNPs and Control animals (Table 5). Moreover, the particles seemed to be retained at the injection site (Fig. 10). Comparing the distribution of the two Cores, Core 1 AuNPs seemed to be distributed in a more disperse way, whereas Core 2 AuNPs appeared to have a "vessel-like" shape distribution. The reason behind this different distribution is not fully understood, however it is hypothesized that it might be a consequence of the overall AuNP features and how they interact with biological entities. Size can be pointed out as one of the reasons possibly behind such observations, as typically smaller particles can diffuse easily and are less opsonized than larger counterparts (Lin et al., 2015), agreeing with what was here observed, as Core 1 AuNPs are smaller than Core 2 AuNPs.

Histopathological analyses supported the macroscopical observations: no signs of lesion in any of the analyzed organs were observed (Figure S5 from supplementary material in Appendix A).

Table 5
Tissue indexes of healthy female BALB/c mice from each test group.

Test Group		Organ		
	Time after injection	Liver	Spleen	Kidneys
Control	———	23.3 ± 0.1	6.5 ± 0.1	12.4 ± 0.4
Core 1 AuNPs	4 h	22.9 ± 0.7	6.2 ± 0.1	11.7 ± 0.1
	24 h	23.9 ± 0.3	5.8 ± 0.3	12.2 ± 0.2
	48 h	22.7 ± 0.3	6.4 ± 0.2	12.0 ± 0.2
Core 2 AuNPs	4 h	23.3 ± 0.6	6.1 ± 0.1	12.4 ± 0.1
	24 h	22.8 ± 0.1	5.9 ± 0.3	11.8 ± 0.3
	48 h	21.9 ± 0.3	5.6 ± 0.2	11.0 ± 0.5

Data represented as mean ± SD, n ≥ 2.

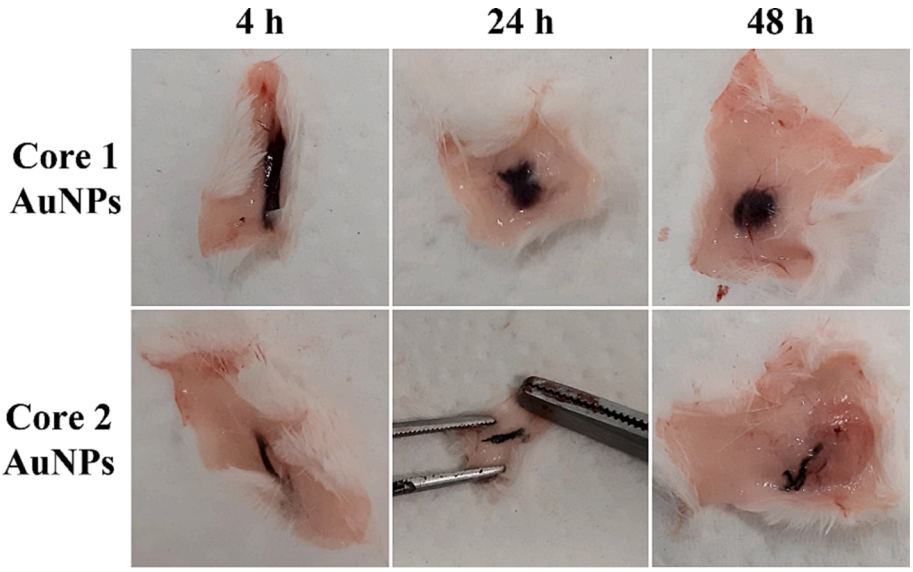

Fig. 10. Representative photographs of the local of injection of Core 1 and Core 2 AuNPs at different time points after injection.

Lastly, as supportive evidence of the local retention of the AuNPs at injection site, the biodistribution of the AuNPs at different timepoints after injection was assessed by quantification of the Au element by ICP analysis. Results showed that a neglectable percentage of the injected dose was capable of surpassing the injection site (Table 6) since the majority (practically all AuNPs) of the injected dose was found at injection site. Fig. 10 shows representative pictures indicative of that retention. Such results are quite promising for an intratumoral injection of the AuNPs, once they might be indicative that AuNPs most likely will stay at the tumor site, enhancing the therapeutic effect while minimizing undesirable side effects and systemic toxicity. Moreover, these results make it possible to consider the hypothesis of applying multiple-irradiation cycles using a single AuNP injection. Yet, it must be noticed that moving forward to a multiple-irradiation cycle treatment following a single intratumor AuNPs injection still lacks the repetition of the same assay after an intratumor administration of the AuNPs to assess if tumor vasculature and microenvironment leds to different outcomes.

In order to clearly assess the AuNPs retention at the injection site in live animals, mice were injected with the two most promising Core AuNPs and were subjected to CT. Animals showed local retention of the AuNPs at injection site up to 1 month after administration of the AuNPs (Fig. 11). None of the animals showed any sign of suffering or lack of welfare, thus confirming the safety of AuNPs administration. These results reinforce the previously referred interest in applying multi-irradiation cycles after a single AuNPs' administration. Nonetheless, the importance of studying the AuNPs' long-term toxicity and clearance cannot be neglected. State of the art on AuNPs notices the limited secretion and clearance of AuNPs from *in vivo* models, with the majority of the studies reporting liver and spleen accumulation (Adewale et al., 2019; De Jong et al., 2008; Lin et al., 2015). Nevertheless, AuNPs' features, such as size, shape, coating and functionalization, and the chosen administration routes are known to play an active role on the AuNPs fate *in vivo* (Adewale et al., 2019; De Jong et al., 2008; Lin et al., 2015). Small AuNPs (<6 nm) were proved to be secreted through urine (Semmler-Behnke et al., 2008; Zhou et al., 2011). However, larger AuNPs cannot be easily secreted and were already reported to be accumulated in the liver up to 6 months post-administration, with no mention to any toxicity (Sadauskas et al., 2009). In addition, in the case of the specific application herein reported, the AuNPs fate might also depend on the treatment modality applied. In the case of a combined PTT-surgery strategy, the particles might be removed from the organism together with the resected dead tumor cells.

Table 6
Percentage of the injected dose of gold (based on ICP-OES analysis) at the injection site and blood, 4 h, 24 h and 48 h post-s.c. administration of Core 1 and Core 2 AuNPs. Results are presented as mean ± SD, n = 3.

Test Group		Au quantity (% of injected dose)	
	Time after injection	Injection site	Blood
Core 1 AuNPs	4 h	111.9 ± 0.9	0.2 ± 0.2
	24 h	88.4 ± 3.9	0.4 ± 0.1
	48 h	100.4 ± 14.6	0.3 ± 0.1
Core 2 AuNPs	4 h	113.4 ± 6.9	0.3 ± 0.3
	24 h	108.4 ± 15.3	0.5 ± 0.2
	48 h	126.4 ± 13.0	0.5 ± 0.1

3.2.7. Preliminary in vitro PTT efficacy using 2D culture of 4 T1, MCF-7 and HaCaT cells

The safety and efficacy of the two most promising Core AuNPs were further assessed in 2D cultures of commercialized cell lines when combined with NIR laser irradiation through MTT assay (Fig. 12). Core 2 AuNPs alone prove to be completely safe in all cell lines tested. By its turn, Core 1 AuNPs led to a slight reduction of MCF-7 and HaCaT cells' viability (8 % and 15 %, respectively) even though they did not affect 4T1 cells. Nevertheless, the decrease in viability is not considered toxic attending the cytotoxicity definition from ISO 10993–5:2009 (E), which states that a product or formulation is considered cytotoxic when the cellular viability is reduced in more than 30 %. By its turn laser irradiation *per se* was also unable to reduce the cells' viability, regardless the cell line. In fact, it actually slightly increased the cells' viability, especially in the case of HaCaT cells. When assessing the actual photothermal effect of the AuNPs *in vitro* the two cores behaved quite differently. When combining Core 1 AuNPs incubation with posterior NIR laser irradiation, no significant 4T1 cells' viability reduction was observed. In turn, MCF-7 and HaCaT cells showed a minor viability reduction when comparing to Controls (11 % and 7 %, respectively), but it was not considered a cytotoxic effect. A different scenario was observed when Core 2 AuNPs were combined with laser irradiation, as it resulted in cells' viability reduction superior to 70 % both in 4T1 and MCF-7 cells. As for HaCaT, the cell viability reduction caused by the combination of Core 2 AuNPs with laser irradiation was somewhat lower (44 %). Overall, these results prove that both AuNPs and laser irradiation alone are unable to result in a significant cell death. Moreover, Core 1 AuNPs

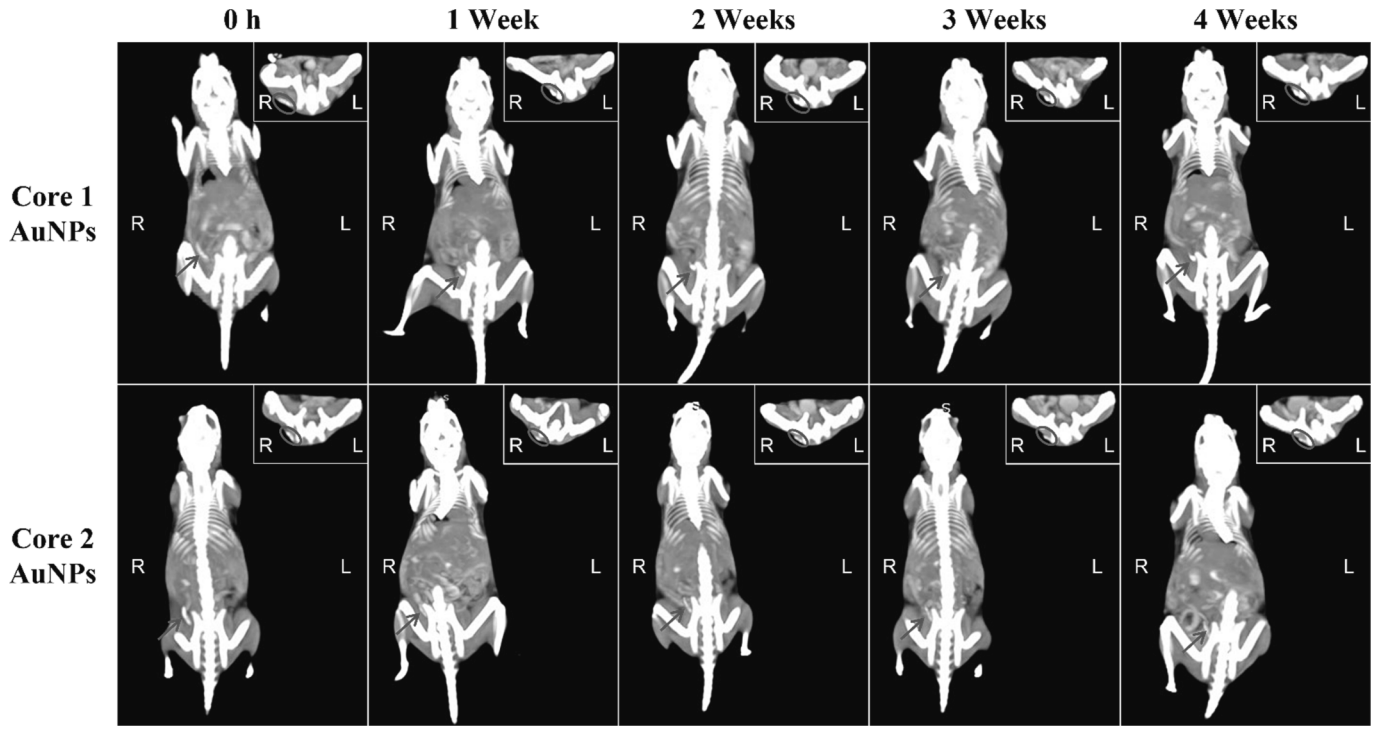

Fig. 11. Representative *in vivo* CT images of mice showing local accumulation of Core 1 and Core 2 AuNPs at injection site at different timepoints after injection (from 0 h up to 1 month). Red arrows and circles point out the AuNPs accumulations in coronal and axial images, respectively. R indicates the right and L the left sides of the animals. (For interpretation of the references to color in this figure legend, the reader is referred to the web version of this article.)

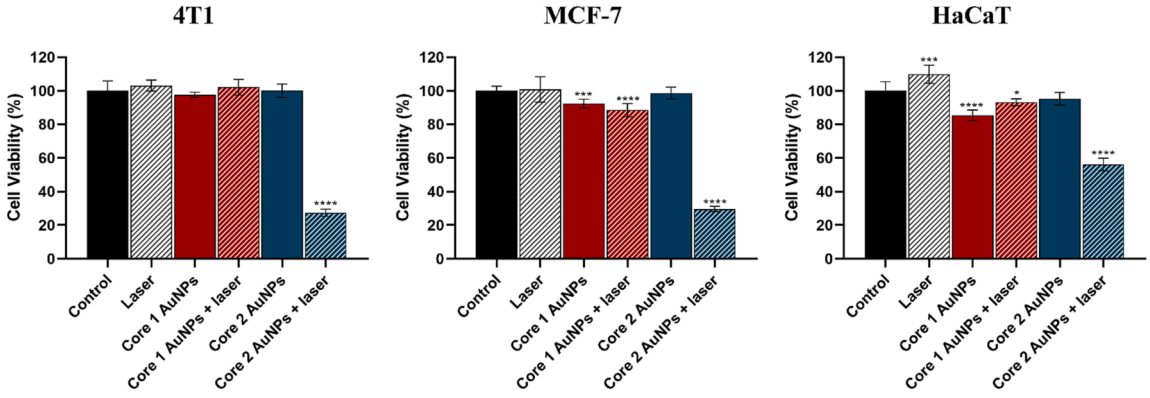

Fig. 12. Cell viability (%) of 4T1, MCF-7 and HaCaT cells non-treated (Control - black columns) and treated with: 5 min of NIR laser irradiation (black and white stripped columns); Core 1 AuNPs (red full columns); Core 1 AuNPs + 5 min of NIR laser irradiation (red stripped columns); Core 2 AuNPs (blue full columns); Core 2 AuNPs + 5 min of NIR laser irradiation (blue stripped columns). Data represented as mean ± SD, n > 4. Statistical significance is represented as * $p < 0.05$, *** $p < 0.001$, and **** $p < 0.0001$ comparing with Control cells. (For interpretation of the references to color in this figure legend, the reader is referred to the web version of this article.)

also prove to be insufficient to result in cell death when combined with laser irradiation. Contrarily, Core 2 AuNPs proved to be strong photothermal enhancers when combined with NIR laser irradiation, resulting in high cell death. In addition, the cell death observed for breast cancer cells, both human and murine, was fairly more pronounced than the observed for keratinocytes. This last observation is supported by data from the literature reporting higher sensitivity of cancer cells to heat than healthy cells (Huang et al., 2008; Pérez-Hernández, 2018). Altogether, these results proved the high potential of the produced Core 2 AuNPs to be used as strong PTT enhancers.

Comparing the results herein observed with other works from the literature is quite difficult, as the *in vitro* photothermal efficacy depends on multiples variables such as AuNPs concentration, overall AuNPs features, laser irradiation and exposure time, etc… (Cao et al., 2016; Xu et al., 2019b,a). In addition, such results also depend on the cell lines tested (Kang et al., 2017). As an example, Xu and colleagues showed that gold nanocages coated with hyaluronic acid with sizes around 190 nm at a concentration of 50 μg/mL were able to cause a 26 % reduction of 4T1 cell's viability when irradiated with a 808 nm laser at 0.35 W/cm^2 for 10 min (X. Xu et al., 2019). For comparison, Core 2 AuNPs present comparable size to the reported nanocages, and at a similar concentration (250 μM of Au can be approximated to 49 μg/mL of Au) were able to cause 4T1 cell's viability reduction superior to 70 % when an irradiation with a 808 nm laser at 7.96 W/cm^2 took place for 5 min. Thus, Core 2 AuNPs showed superior cancer cell killing in the same cell line than similar sized nanoparticles with a different shape and functionalization at comparable concentrations, using shorter irradiation periods, although the irradiance applied here was superior. In another example

studying the synergistic effect of gold nanorods coated with porphyrin and trastuzumab (as anti-HER-2 receptor), Kang et al. reported that concentrations > 100 μg/mL and > 50 μg/mL were needed to cause a reduction of BT474 cells viability higher than 50 % when exposing the cells to 5 min irradiation with a 808 nm laser at 6.07 W/cm^2 and 13.6 W/cm^2, respectively (Kang et al., 2017). The same work also tested the systems' PTT efficacy in SKBR3 cells and it was observed that for the same exposure time, when an irradiance of 6.07 W/cm^2 was used, the cells viability was still higher than 50 % even when a concentration of 200 μg/mL of gold nanorods was used (Kang et al., 2017). Moreover, when the laser dose was increased up to 13.6 W/cm^2, SKBR3 cells' viability was only reduced more than 50 % for nanorods' concentrations > 100 μg/mL (Kang et al., 2017). Thus, the results herein reported for Core 2 AuNPs seemed to outstand the results observed for the synergistic effect of the gold nanorods at higher concentrations and laser irradiation doses. Nevertheless, it must be noticed that this comparison not only differs in terms of cell lines, but also in terms of particles shape and size, as Core 2 AuNPs are mostly quasi-spherical with diameter ≈ 190 nm and the gold nanorods presented sizes ≈ 40 nm x 10 nm. Thus, overall, the results herein reported are very encouraging, despite the challenging comparison with other published works.

4. Conclusions and future work

This work gathers an extensive characterization of Core AuNPs synthesized in order to optimize their features and maximize their potential as photothermal therapy enhancers when combined with a NIR laser irradiation. Physicochemical, photothermal and biological profiles of tested AuNPs unveil their undeniable value as part of a PTT system to fight superficial and localized tumors, such as breast tumors. Among the Core AuNPs prepared, Core 2 AuNPs showed the ability to increase phantoms temperature up to 19 °C when irradiated with a NIR laser. In addition, after demonstrated the safety of Core 2 AuNPs *in vivo*, it was also revealed their ability to be locally retained in the injection site up to 1 month post administration. At last, Core 2 AuNPs evidenced high photothermal potential when combined with short periods of NIR laser irradiation (5 min), as they resulted in cell viability reduction superior to 70 % in both murine and human commercialized breast cancer cells. Further tests are, however, required to evaluate *in vivo* safety and efficacy of the proposed PTT system.

CRediT authorship contribution statement

Tânia Ferreira-Gonçalves: Conceptualization, Formal analysis, Investigation, Methodology, Roles/Writing – original draft, Writing – review & editing. **Daniela Nunes:** Formal analysis, Methodology, Roles/Writing – original draft, Writing – review & editing. **Elvira Fortunato:** Funding acquisition, Resources, Writing – review & editing. **Rodrigo Martins:** Funding acquisition, Resources, Writing – review & editing. **António P. de Almeida:** Methodology, Resources, Writing – review & editing. **Lina Carvalho:** Formal analysis, Methodology, Resources. **David Ferreira:** Supervision, Writing – review & editing. **José Catarino:** Formal analysis, Methodology, Writing – review & editing. **Pedro Faísca:** Formal analysis, Methodology, Resources, Writing – review & editing. **Hugo A. Ferreira:** Supervision, Writing – review & editing. **M. Manuela Gaspar:** Funding acquisition, Resources, Writing – review & editing. **João M.P. Coelho:** Conceptualization, Funding acquisition, Project administration, Resources, Writing – review & editing. **Catarina Pinto Reis:** Conceptualization, Funding acquisition, Project administration, Resources, Supervision, Writing – review & editing.

Declaration of competing interest

The authors declare that they have no known competing financial interests or personal relationships that could have appeared to influence the work reported in this paper.

Data availability

Data will be made available on request.

Acknowledgements

The authors are thankful to Fundação para a Ciência e a Tecnologia, I.P. (FCT, Portugal) for the essential financial support under project references UIDB/00645/2020, UIDP/00645/2020 UIDB/04138/2020, UIDP/04138/2020 and PTDC/QUI-QIN/0586/2020. Moreover, the authors also thank FCT for the financial support in the scope of the project's LA/P/0037/2020, UIDP/50025/2020, and UIDB/50025/2020 of the Associate Laboratory Institute of Nanostructures, Nanomodelling, and Nanofabrication-i3N. Acknowledgments also go to the European Comission with the funded project SYNERGY H2020-WIDESPREAD-2020-5, CSA, proposal n° 952169, EMERGE-2020-INFRAIA-2020-1, proposal n° 101008701, and to the European Community's H2020 program under grant agreement No. 787410 (European Research Council, ERC-2018-AdG DIGISMART). T.F.-G. would like to thank FCT as well, for the PhD Fellowship SFRH/BD/147306/2019.

Appendix A. Supplementary data

Supplementary data to this article can be found online at https://doi.org/10.1016/j.ijpharm.2023.123659.

References

Abadeer, N.S., Murphy, C.J., 2016. Recent progress in cancer thermal therapy using gold nanoparticles. J. Phys. Chem. C 120, 4691–4716. https://doi.org/10.1021/acs.jpcc.5b11232.

Adewale, O.B., Davids, H., Cairncross, L., Roux, S., 2019. Toxicological behavior of gold nanoparticles on various models: Influence of physicochemical properties and other factors. Int. J. Toxicol. 38, 357–384. https://doi.org/10.1177/1091581819863130.

Alkilany, A.M., Murphy, C.J., 2010. Toxicity and cellular uptake of gold nanoparticles: What we have learned so far? J. Nanoparticle Res. 12, 2313–2333. https://doi.org/10.1007/s11051-010-9911-8.

Alrahili, M., Savchuk, V., McNear, K., Pinchuk, A., 2020. Absorption cross section of gold nanoparticles based on NIR laser heating and thermodynamic calculations. Sci. Rep. 10, 1–9. https://doi.org/10.1038/s41598-020-75895-9.

Amaral, M., Charmier, A.J., Afonso, R.A., Catarino, J., Faísca, P., Carvalho, L., Ascensão, L., Coelho, J.M.P., Manuela Gaspar, M., Reis, C.P., 2021. Gold-based nanoplatform for the treatment of anaplastic thyroid carcinoma: A step forward. Cancers (basel). 13, 1–24. https://doi.org/10.3390/cancers13061242.

Amendola, V., Pilot, R., Frasconi, M., Maragò, O.M., Iatì, M.A., 2017. Surface plasmon resonance in gold nanoparticles: a review. J. Phys. Condens. Matter 29 (20), 203002.

Arellano, L.G., Villar-Alvarez, E.M., Velasco, B., Domínguez-Arca, V., Prieto, G., Cambón, A., Barbosa, S., Taboada, P., 2023. Light excitation of gold Nanorod-Based hybrid nanoplatforms for simultaneous bimodal phototherapy. J. Mol. Liq. 377, 121511 https://doi.org/10.1016/j.molliq.2023.121511.

Ayala-Orozco, C., Urban, C., Knight, M.W., Urban, A.S., Neumann, O., Bishnoi, S.W., Mukherjee, S., Goodman, A.M., Charron, H., Mitchell, T., Shea, M., Roy, R., Nanda, S., Schiff, R., Halas, N.J., Joshi, A., 2014. Au nanomatryoshkas as efficient near-infrared photothermal transducers for cancer treatment: Benchmarking against nanoshells. ACS Nano 8, 6372–6381. https://doi.org/10.1021/nn501871d.

Bai, X., Wang, Y., Song, Z., Feng, Y., Chen, Y., Zhang, D., Feng, L., 2020. The basic properties of gold nanoparticles and their applications in tumor diagnosis and treatment. Int. J. Mol. Sci. 21, 2480. https://doi.org/10.3390/ijms21072480.

Bashkatov, A.N., Genina, E.A., Kochubey, V.I., Tuchin, V.V., 2005. Optical properties of human skin, subcutaneous and mucous tissues in the wavelength range from 400 to 2000 nm. J. Phys. D. Appl. Phys. 38, 2543–2555. https://doi.org/10.1088/0022-3727/38/15/004.

Bootz, A., Vogel, V., Schubert, D., Kreuter, J., 2004. Comparison of scanning electron microscopy, dynamic light scattering and analytical ultracentrifugation for the sizing of poly(butyl cyanoacrylate) nanoparticles. Eur. J. Pharm. Biopharm. 57, 369–375. https://doi.org/10.1016/S0939-6411(03)00193-0.

Bouché, M., Hsu, J.C., Dong, Y.C., Kim, J., Taing, K., Cormode, D.P., 2020. Recent Advances in Molecular Imaging with Gold Nanoparticles. Bioconjug. Chem. 31, 303–314. https://doi.org/10.1021/acs.bioconjchem.9b00669.

Brust, M., Walker, M., Bethell, D., Schiffrin, D.J., Whyman, R., 1994. Synthesis of thiol-derivatised gold nanoparticles in a two-phase Liquid-Liquid system. J. Chem. Soc. Chem. Commun. 0 (7), 801–802. https://doi.org/10.1039/C39940000801.

Cao, F., Yao, Q., Yang, T., Zhang, Z., Han, Y., Feng, J., Wang, X.H., 2016. Marriage of antibody-drug conjugate with gold nanorods to achieve multi-modal ablation of

breast cancer cells and enhanced photoacoustic performance. RSC Adv. 6, 46594–46606. https://doi.org/10.1039/c6ra01557c.
Ciccone, V., Terzuoli, E., Donnini, S., Giachetti, A., Morbidelli, L., Ziche, M., 2018. Stemness marker ALDH1A1 promotes tumor angiogenesis via retinoic acid/HIF-1α/VEGF signalling in MCF-7 breast cancer cells. J. Exp. Clin. Cancer Res. 37, 1–16. https://doi.org/10.1186/s13046-018-0975-0.
Costa, E., Ferreira-Gonçalves, T., Cardoso, M., Coelho, J.M.P., Gaspar, M.M., Faísca, P., Ascensão, L., Cabrita, A.S., Reis, C.P., Figueiredo, I.V., 2020. A step forward in breast cancer research: From a natural-like experimental model to a preliminary photothermal approach. Int. J. Mol. Sci. 21, 1–28. https://doi.org/10.3390/ijms21249681.
Daems, N., Michiels, C., Lucas, S., Baatout, S., Aerts, A., 2021. Gold nanoparticles meet medical radionuclides. Nucl. Med. Biol. 100–101, 61–90. https://doi.org/10.1016/j.nucmedbio.2021.06.001.
Danaei, M., Dehghankhold, M., Ataei, S., Davarani, F.H., Javanmard, R., Dokhani, A., Khorasani, S., Mozafari, M.R., 2018. Impact of Particle Size and Polydispersity Index on the Clinical Applications of Lipidic Nanocarrier Systems. Pharmaceutics 10, 1–17. https://doi.org/10.3390/pharmaceutics10020057.
De Jong, W.H., Hagens, W.I., Krystek, P., Burger, M.C., Sips, A.J.A.M., Geertsma, R.E., 2008. Particle size-dependent organ distribution of gold nanoparticles after intravenous administration. Biomaterials 29, 1912–1919. https://doi.org/10.1016/j.biomaterials.2007.12.037.
De Souza, C.D., Ribeiro Nogueira, B., Rostelato, M.E.C.M., 2019. Review of the methodologies used in the synthesis gold nanoparticles by chemical reduction. J. Alloys Compd. 798, 714–740. https://doi.org/10.1016/j.jallcom.2019.05.153.
Deng, X., Shao, Z., Zhao, Y., 2021. Solutions to the Drawbacks of Photothermal and Photodynamic Cancer Therapy. Adv. Sci. 8, 2002504. https://doi.org/10.1002/advs.202002504.
Eissa, A.S., 2019. Effect of SDS on whey protein polymers. Molecular investigation via dilute solution viscometry and dynamic light scattering. Food Hydrocoll. 87, 97–100. https://doi.org/10.1016/j.foodhyd.2018.07.046.
Faraday, M., 1857. X. The Bakerian Lecture. - Experimental relations of gold (and other metals) to light. Philos. Trans. R. Soc. London 147, 145–181. https://doi.org/10.1098/rstl.1857.0011.
Fazal, S., Jayasree, A., Sasidharan, S., Koyakutty, M., Nair, S.V., Menon, D., 2014. Green Synthesis of Anisotropic Gold Nanoparticles for Photothermal Therapy of Cancer. ACS Appl. Mater. Interfaces 6, 8080–8089. https://doi.org/10.1021/am500302t.
Ferreira-Gonçalves, T., Ferreira, D., Ferreira, H.A., Reis, C.P., 2021. Nanogold-based materials in medicine: From their origins to their future. Nanomedicine 16, 2695–2723. https://doi.org/10.2217/nnm-2021-0265.
Ferreira-Gonçalves, T., Gaspar, M.M., Coelho, J.M.P., Marques, V., Viana, A.S., Ascensão, L., Carvalho, L., Rodrigues, C.M.P., Ferreira, H.A., Ferreira, D., Reis, C.P., 2022. The Role of Rosmarinic Acid on the Bioproduction of Gold Nanoparticles as Part of a Photothermal Approach for Breast Cancer Treatment. Biomolecules 12, 71. https://doi.org/10.3390/biom12010071.
Frens, G., 1973. Controlled Nucleation for the Regulation of the Particle Size in Monodisperse Gold Suspensions. Nat. Phys. Sci. 241, 20–22. https://doi.org/10.1038/physci241020a0.
Fröhlich, E., 2012. The role of surface charge in cellular uptake and cytotoxicity of medical nanoparticles. Int. J. Nanomedicine 7, 5577–5591. https://doi.org/10.2147/IJN.S36111.
Geneva, I.I., Cuzzo, B., Fazili, T., Javaid, W., 2019. Normal body temperature: A systematic review. Open Forum. Infect. Dis. 6, ofz032. https://doi.org/10.1093/ofid/ofz032.
Habashi, F., 2016. Gold – An Historical Introduction. Gold Ore Process. 1–20 https://doi.org/10.1016/b978-0-444-63658-4.00001-3.
Habib, A., Tabata, M., Wu, Y.G., 2005. Formation of gold nanoparticles by Good's Buffers. Bull. Chem. Soc. Jpn. 78, 262–269. https://doi.org/10.1246/bcsj.78.262.
Hillyer, J.F., Albrecht, R.M., 2001. Gastrointestinal persorption and tissue distribution of differently sized colloidal gold nanoparticles. J. Pharm. Sci. 90, 1927–1936. https://doi.org/10.1002/jps.1143.
Honary, S., Zahir, F., 2013. Effect of zeta potential on the properties of nano-drug delivery systems - a review (Part 2). Trop. J. Pharm. Res. 12, 265–273. https://doi.org/10.4314/tjpr.v12i2.20.
Huang, C.-J., Chiu, P.-H., Wang, Y.-H., Yang, C.-F., 2006. Synthesis of the gold nanodumbbells by electrochemical method. J. Colloid Interface Sci. 303, 430–436. https://doi.org/10.1016/j.jcis.2006.07.073.
Huang, X., Jain, P.K., El-Sayed, I.H., El-Sayed, M.A., 2008. Plasmonic photothermal therapy (PPTT) using gold nanoparticles. Lasers Med. Sci. 23, 217–228. https://doi.org/10.1007/s10103-007-0470-x.
Huang, P., Lin, J., Li, W., Rong, P., Wang, Z., Wang, S., Wang, X., Sun, X., Aronova, M., Niu, G., Leapman, R.D., Nie, Z., Chen, X., 2013. Biodegradable gold nanovesicles with an ultrastrong plasmonic coupling effect for photoacoustic imaging and photothermal therapy. Angew. Chemie Int. Ed. 52, 13958–13964. https://doi.org/10.1002/anie.201308986.
Information card for entry 1100138 [WWW Document], n.d. Crystallogr. Open Database. URL http://www.crystallography.net/cod/1100138.html (accessed 1.12.22).
Jacques, S.L., 2013. Optical properties of biological tissues: a review. Phys. Med. Biol. 58, R37–R61. https://doi.org/10.1088/0031-9155/58/11/R37.
Jana, N.R., Gearheart, L., Murphy, C.J., 2001. Seeding growth for size control of 5–40 nm diameter gold nanoparticles. Langmuir 17, 6782–6786. https://doi.org/10.1021/la0104323.
Jeevanandam, J., Barhoum, A., Chan, Y.S., Dufresne, A., Danquah, M.K., 2018. Review on nanoparticles and nanostructured materials: History, sources, toxicity and regulations. Beilstein J. Nanotechnol. 9, 1050–1074. https://doi.org/10.3762/bjnano.9.98.
Jiang, K., Smith, D.A., Pinchuk, A., 2013. Size-dependent photothermal conversion efficiencies of plasmonically heated gold nanoparticles. J. Phys. Chem. C 117, 27073–27080. https://doi.org/10.1021/jp409067h.
Jiang, X.M., Wang, L.M., Wang, J., Chen, C.Y., 2012. Gold nanomaterials: Preparation, chemical modification, biomedical applications and potential risk assessment. Appl. Biochem. Biotechnol. 166, 1533–1551. https://doi.org/10.1007/s12010-012-9548-4.
Jiang, P., Wang, Y., Zhao, L., Ji, C., Chen, D., Nie, L., 2018. Applications of gold nanoparticles in non-optical biosensors. Nanomaterials 8, 977. https://doi.org/10.3390/nano8120977.
Kang, X., Guo, X., An, W., Niu, X., Li, S., Liu, Z., Yang, Y., Wang, N., Jiang, Q., Yan, C., Wang, H., Zhang, Q., 2017. Photothermal therapeutic application of gold nanorods-porphyrin-trastuzumab complexes in HER2-positive breast cancer. Sci. Rep. 7, 42069. https://doi.org/10.1038/srep42069.
Kim, H.J., Kim, S.H., Kim, H.M., Kim, Y.S., Oh, J.M., 2021. Surface roughness effect on the cellular uptake of layered double hydroxide nanoparticles. Appl. Clay Sci. 202, 105992 https://doi.org/10.1016/j.clay.2021.105992.
Kumari, S., Sharma, N., Sahi, S.V., 2021. Advances in cancer therapeutics: Conventional thermal therapy to nanotechnology-based photothermal therapy. Pharmaceutics 13 (8), 1174. https://doi.org/10.3390/pharmaceutics13081174.
Larm, N.E., Essner, J.B., Pokpas, K., Canon, J.A., Jahed, N., Iwuoha, E.I., Baker, G.A., 2018. Room-temperature turkevich method: Formation of gold nanoparticles at the speed of mixing using cyclic oxocarbon reducing agents. J. Phys. Chem. C 122, 5105–5118. https://doi.org/10.1021/acs.jpcc.7b10536.
Lee, J., Choi, S.U.S., Jang, S.P., Lee, S.Y., 2012. Production of aqueous spherical gold nanoparticles using conventional ultrasonic bath. Nanoscale Res. Lett. 7, 420. https://doi.org/10.1186/1556-276X-7-420.
Lee, K.X., Shameli, K., Yew, Y.P., Teow, S.Y., Jahangirian, H., Rafiee-Moghaddam, R., Webster, T.J., 2020. Recent developments in the facile bio-synthesis of gold nanoparticles (AuNPs) and their biomedical applications. Int. J. Nanomedicine 15, 275–300. https://doi.org/10.2147/IJN.S233789.
Li, N., Zhao, P., Astruc, D., 2014. Anisotropic gold nanoparticles: Synthesis, properties, applications, and toxicity. Angew. Chemie - Int. Ed. 53, 1756–1789. https://doi.org/10.1002/anie.201300441.
Lim, S.H., Park, Y., 2018. Green synthesis, characterization and catalytic activity of gold nanoparticles prepared using rosmarinic acid. J. Nanosci. Nanotechnol. 18, 659–667. https://doi.org/10.1166/jnn.2018.13982.
Lin, Z., Monteiro-Riviere, N.A., Riviere, J.E., 2015. Pharmacokinetics of metallic nanoparticles. Wiley Interdiscip. Rev. Nanomedicine Nanobiotechnology 7, 189–217. https://doi.org/10.1002/wnan.1304.
Lin, J., Zhang, H., Chen, Z., Zheng, Y., 2010. Penetration of lipid membranes by gold nanoparticles: Insights into cellular uptake, cytotoxicity, and their relationship. ACS Nano 4, 5421–5429. https://doi.org/10.1021/nn1010792.
Liu, T.-M., Conde, J., Lipiński, T., Bednarkiewicz, A., Huang, C.-C., 2017. Smart NIR linear and nonlinear optical nanomaterials for cancer theranostics: Prospects in photomedicine. Prog. Mater. Sci. 88, 89–135. https://doi.org/10.1016/j.pmatsci.2017.03.004.
Lopes, J., Coelho, J.M.P., Vieira, P.M.C., Viana, A.S., Gaspar, M.M., Reis, C., 2020. Preliminary assays towards melanoma cells using phototherapy with gold-based nanomaterials. Nanomaterials 10, 1536. https://doi.org/10.3390/nano10081536.
Lopes, J., Ferreira-Gonçalves, T., Figueiredo, I.V., Rodrigues, C.M.P., Ferreira, H., Ferreira, D., Viana, A.S., Faísca, P., Gaspar, M.M., Coelho, J.M.P., Silva, C.O., Reis, C. P., 2021. Proof-of-concept study of multifunctional hybrid nanoparticle system combined with NIR laser irradiation for the treatment of melanoma. Biomolecules 11, 511. https://doi.org/10.3390/biom11040511.
Luminex® [WWW Document], n.d. VERIGENE® Syst. URL https://www.luminexcorp.com/eu/the-verigene-system/ (accessed 6.9.21).
Luo, D., Wang, X., Zeng, S., Ramamurthy, G., Burda, C., Basilion, J.P., 2019. Prostate-specific membrane antigen targeted gold nanoparticles for prostate cancer radiotherapy: Does size matter for targeted particles? Chem. Sci. 10, 8119–8128. https://doi.org/10.1039/c9sc02290b.
Malassis, L., Dreyfus, R., Murphy, R.J., Hough, L.A., Donnio, B., Murray, C.B., 2016. One-step green synthesis of gold and silver nanoparticles with ascorbic acid and their versatile surface post-functionalization. RSC Adv. 6, 33092–33100. https://doi.org/10.1039/c6ra00194g.
Malekzadeh, R., Mortezazadeh, T., Abdulsahib, W.K., Babaye abdollahi, B., Hamblin, M. R., Mansoori, B., Alsaikhan, F., Zeng, B.o., 2023. Nanoarchitecture-based photothermal ablation of cancer: A systematic review. Environ. Res. 236, 116526. https://doi.org/10.1016/j.envres.2023.116526.
Moustaoui, H., Saber, J., Djeddi, I., Liu, Q., Diallo, A.T., Spadavecchia, J., de la Chapelle, M.L., Djaker, N., 2019. Shape and size effect on photothermal heat elevation of gold nanoparticles: absorption coefficient experimental measurement of spherical and urchin-shaped gold nanoparticles. J. Phys. Chem. C 123, 17548–17554. https://doi.org/10.1021/acs.jpcc.9b03122.
Naharuddin, N.Z.A., Sadrolhosseini, A.R., Bakar, M.H.A., Tamchek, N., Mahdi, M.A., 2020. Laser ablation synthesis of gold nanoparticles in tetrahydrofuran. Opt. Mater. Express 10, 323–331. https://doi.org/10.1364/OME.381427.
Ngo, V.K.T., Nguyen, D.G., Huynh, T.P., Lam, Q.V., 2016. A low cost technique for synthesis of gold nanoparticles using microwave heating and its application in signal amplification for detecting Escherichia coli O157:H7 bacteria. Adv. Nat. Sci. Nanosci. Nanotechnol. 7, 035016 https://doi.org/10.1088/2043-6262/7/3/035016.
Nguyen, N.H.A., Falagan-Lotsch, P., 2023. Mechanistic insights into the biological effects of engineered nanomaterials: A focus on gold nanoparticles. Int. J. Mol. Sci. 24, 4109. https://doi.org/10.3390/ijms24044109.

Nguyen, P.D., Zhang, X., Su, J., 2019. One-step controlled synthesis of size-tunable toroidal gold particles for biochemical sensing. ACS Appl. Nano Mater. 2, 7839–7847. https://doi.org/10.1021/acsanm.9b01856.
Niculescu, A., Grumezescu, A.M., 2021. Photodynamic Therapy — An Up-to-Date Review. Appl. Sci. 11, 3626. https://doi.org/10.3390/app11083626.
Ortiz-Castillo, J.E., Gallo-Villanueva, R.C., Madou, M.J., Perez-Gonzalez, V.H., 2020. Anisotropic gold nanoparticles: A survey of recent synthetic methodologies. Coord. Chem. Rev. 425, 213489 https://doi.org/10.1016/j.ccr.2020.213489.
Paramasivam, G., Kayambu, N., Rabel, A.M., Sundramoorthy, A.K., Sundaramurthy, A., 2017. Anisotropic noble metal nanoparticles: Synthesis, surface functionalization and applications in biosensing, bioimaging, drug delivery and theranostics. Acta Biomater. 49, 45–65. https://doi.org/10.1016/j.actbio.2016.11.066.
Park, J., Lee, Y.K., Park, I.K., Hwang, S.R., 2021. Current limitations and recent progress in nanomedicine for clinically available photodynamic therapy. Biomedicines 9, 1–17. https://doi.org/10.3390/biomedicines9010085.
Park, H., Yang, J., Seo, S., Kim, K., Suh, J., Kim, D., Haam, S., Yoo, K.-H., 2008. Multifunctional nanoparticles for photothermally controlled drug delivery and magnetic resonance imaging enhancement. Small 4, 192–196. https://doi.org/10.1002/smll.200700807.
Pattani, V.P., Tunnell, J.W., 2012. Nanoparticle-mediated photothermal therapy: A comparative study of heating for different particle types. Lasers Surg. Med. 44, 675–684. https://doi.org/10.1002/lsm.22072.
Pérez-Hernández, M., 2018. Mechanisms of Cell Death Induced by Optical Hyperthermia. In: Nanomaterials for Magnetic and Optical Hyperthermia Applications, pp. 201–228. https://doi.org/10.1016/B978-0-12-813928-8.00008-9.
Piloni, A., Wong, C.K., Chen, F., Lord, M., Walther, A., Stenzel, M.H., 2019. Surface roughness influences the protein corona formation of glycosylated nanoparticles and alter their cellular uptake. Nanoscale 11, 23259–23267. https://doi.org/10.1039/c9nr06835j.
Pu, Y., Zhao, Y., Zheng, P., Li, M., 2018. Elucidating the Growth Mechanism of Plasmonic Gold Nanostars with Tunable Optical and Photothermal Properties. Inorg. Chem. 57, 8599–8607. https://doi.org/10.1021/acs.inorgchem.8b01354.
Qin, Z., Wang, Y., Randrianalisoa, J., Raeesi, V., Chan, W.C.W., Lipinski, W., Bischof, J. C., 2016. Quantitative comparison of photothermal heat generation between gold nanospheres and nanorods. Sci. Rep. 6, 29836. https://doi.org/10.1038/srep29836.
Rajabi, S., Ramazani, A., Hamidi, M., Naji, T., 2015. Artemia salina as a model organism in toxicity assessment of nanoparticles. DARU. J. Pharm. Sci. 23, 1–6. https://doi.org/10.1186/s40199-015-0105-x.
Rechendorff, K., Hovgaard, M.B., Foss, M., Zhdanov, V.P., Besenbacher, F., 2006. Enhancement of protein adsorption induced by surface roughness. Langmuir 22, 10885–10888. https://doi.org/10.1021/la0621923.
Reddy, A.S., Chen, C.-Y., Chen, C.-C., Jean, J.-S., Chen, H.-R., Tseng, M.-J., Fan, C.-W., Wang, J.-C., 2010. Biological synthesis of gold and silver nanoparticles mediated by the bacteria Bacillus subtilis. J. Nanosci. Nanotechnol. 10, 6567–6574. https://doi.org/10.1166/jnn.2010.2519.
Research, G.V., n.d. Gold Nanoparticles Market Size, Share & Trends Analysis Report By End-use (Medical & Dentistry, Electronics, Catalysis), By Region, And Segment Forecasts, 2023 - 2030 [WWW Document]. URL https://www.grandviewresearch.com/industry-analysis/gold-nanoparticles-industry# (accessed 10.13.23).
Rijo, P., Batista, M., Matos, M., Rocha, H., Jesus, S., Simões, M.F., 2012. Screening of antioxidant and antimicrobial activities on Plectranthus spp. extracts. Biomed. Biopharm. Res. 9, 225–235.
Riley, R.S., Day, E.S., 2017. Gold nanoparticle-mediated photothermal therapy: applications and opportunities for multimodal cancer treatment. Wiley Interdiscip. Rev. Nanomedicine Nanobiotechnology 9. https://doi.org/10.1002/wnan.1449.
Roper, D.K., Ahn, W., Hoepfner, M., 2007. Microscale heat transfer transduced by surface plasmon resonant gold nanoparticles. J. Phys. Chem. C 111, 3636–3641. https://doi.org/10.1021/jp064341w.
Roy, A., Pandit, C., Gacem, A., Alqahtani, M.S., Bilal, M., Islam, S., Hossain, M.J., Jameel, M., Aruni, W., 2022. Biologically Derived Gold Nanoparticles and Their Applications. Bioinorg. Chem. Appl. 1–13. https://doi.org/10.1155/2022/8184217.
Sadauskas, E., Danscher, G., Stoltenberg, M., Vogel, U., Larsen, A., Wallin, H., 2009. Protracted elimination of gold nanoparticles from mouse liver. Nanomedicine Nanotechnology. Biol. Med. 5, 162–169. https://doi.org/10.1016/j.nano.2008.11.002.
Salehpour, F., Cassano, P., Rouhi, N., Hamblin, M.R., De Taboada, L., Farajdokht, F., Mahmoudi, J., 2019. Penetration Profiles of Visible and Near-Infrared Lasers and Light-Emitting Diode Light through the Head Tissues in Animal and Human Species: A Review of Literature. Photobiomodulation, Photomedicine, Laser Surg. 37, 581–595. https://doi.org/10.1089/photob.2019.4676.
Sarkar, A., Shukla, S.P., Adhikari, S., Mukherjee, T., 2010. Synthesis, stabilisation and surface modification of gold and silver nanoparticles by rosmarinic acid and its analogues. Int. J. Nanotechnol. 7, 1027–1037. https://doi.org/10.1504/IJNT.2010.034707.
Savage, N., 2013. Resources: Mine, all mine! Nature 495, S2–S3. https://doi.org/10.1038/495S2a.
Schleh, C., Semmler-Behnke, M., Lipka, J., Wenk, A., Hirn, S., Schäffler, M., Schmid, G., Simon, U., Kreyling, W.G., 2012. Size and surface charge of gold nanoparticles determine absorption across intestinal barriers and accumulation in secondary target organs after oral administration. Nanotoxicology 6, 36–46. https://doi.org/10.3109/17435390.2011.552811.
Schrade, A., Mailänder, V., Ritz, S., Landfester, K., Ziener, U., 2012. Surface Roughness and Charge Influence the Uptake of Nanoparticles: Fluorescently Labeled Pickering-Type Versus Surfactant-Stabilized Nanoparticles. Macromol. Biosci. 12, 1459–1471. https://doi.org/10.1002/mabi.201200166.
Schrörs, B., Boegel, S., Albrecht, C., Bukur, T., Bukur, V., Holtsträter, C., Ritzel, C., Manninen, K., Tadmor, A.D., Vormehr, M., Sahin, U., Löwer, M., 2020. Multi-Omics Characterization of the 4T1 Murine Mammary Gland Tumor Model. Front. Oncol. 10, 1–14. https://doi.org/10.3389/fonc.2020.01195.
Semmler-Behnke, M., Kreyling, W.G., Lipka, J., Fertsch, S., Wenk, A., Takenaka, S., Schmid, G., Brandau, W., 2008. Biodistribution of 1.4- and 18-nm gold particles in rats. Small 4, 2108–2111. https://doi.org/10.1002/smll.200800922.
Semmler-Behnke, M., Lipka, J., Wenk, A., Hirn, S., Schäffler, M., Tian, F., Schmid, G., Oberdörster, G., Kreyling, W.G., 2014. Size dependent translocation and fetal accumulation of gold nanoparticles from maternal blood in the rat. Part. Fibre Toxicol. 11, 1–12. https://doi.org/10.1186/s12989-014-0033-9.
Sengani, M., Grumezescu, A.M., Rajeswari, V.D., 2017. Recent trends and methodologies in gold nanoparticle synthesis – A prospective review on drug delivery aspect. OpenNano 2, 37–46. https://doi.org/10.1016/j.onano.2017.07.001.
Shankar, S.S., Rai, A., Ahmad, A., Sastry, M., 2004. Rapid synthesis of Au, Ag, and bimetallic Au core-Ag shell nanoparticles using Neem (Azadirachta indica) leaf broth. J. Colloid Interface Sci. 275, 496–502. https://doi.org/10.1016/j.jcis.2004.03.003.
Shen, Q., Min, Q., Shi, J., Jiang, L., Hou, W., Zhu, J.J., 2011. Synthesis of stabilizer-free gold nanoparticles by pulse sonoelectrochemical method. Ultrason. Sonochem. 18, 231–237. https://doi.org/10.1016/j.ultsonch.2010.05.011.
Sheng, W., He, S., Seare, W.J., Almutairi, A., 2017. Review of the progress toward achieving heat confinement—the holy grail of photothermal therapy. J. Biomed. Opt. 22 (8), 080901. https://doi.org/10.1117/1.JBO.22.8.080901.
Sheth, R.A., Wen, X., Li, J., Melancon, M.P., Ji, X., Andrew Wang, Y., Hsiao, C.H., Chow, D.S.L., Whitley, E.M., Li, C., Gupta, S., 2020. Doxorubicin-loaded hollow gold nanospheres for dual photothermal ablation and chemoembolization therapy. Cancer Nanotechnol. 11, 1–16. https://doi.org/10.1186/s12645-020-00062-8.
Shrestha, S., Cooper, L.N., Andreev, O.A., Reshetnyak, Y.K., Antosh, M.P., 2016. Gold Nanoparticles for Radiation Enhancement in Vivo. Jacobs J. Radiat. Oncol. 3, 1–19.
Silva, C.O., Petersen, S.B., Reis, C.P., Rijo, P., Molpeceres, J., Fernandes, A.S., Gonçalves, O., Gomes, A.C., Correia, I., Vorum, H., Neves-Petersen, M.T., Antopolsky, M., 2016a. EGF Functionalized Polymer-Coated Gold Nanoparticles Promote EGF Photostability and EGFR Internalization for Photothermal Therapy. PLoS One 11 (10), e0165419. https://doi.org/10.1371/journal.pone.0165419.
Silva, C.O., Rijo, C., Molpeceres, J., Ascensão, L., Roberto, A., Fernandes, A.S., Gomes, R., Pinto Coelho, J.M., Gabriel, A., Vieira, P., Pinto Reis, C., 2016b. Bioproduction of gold nanoparticles for photothermal therapy. Ther. Deliv. 7, 287–304. https://doi.org/10.4155/tde-2015-0011.
Singh, N., Nayak, J., Patel, K., Sahoo, S.K., Kumar, R., 2018. Electrochemical impedance spectroscopy reveals a new mechanism based on competitive binding between Tris and protein on a conductive biomimetic polydopamine surface. Phys. Chem. Chem. Phys. 20, 25812–25821. https://doi.org/10.1039/c8cp05391j.
Singh, N., Marets, C., Boudon, J., Millot, N., Saviot, L., Maurizi, L., 2021. In vivo protein corona on nanoparticles: does the control of all material parameters orient the biological behavior? Nanoscale Adv. 3, 1209–1229. https://doi.org/10.1039/d0na00863j.
Slepička, P., Kasálková, N.S., Siegel, J., Kolská, Z., Švorčík, V., 2020. Methods of gold and silver nanoparticles preparation. Materials (basel). 13, 1. https://doi.org/10.3390/ma13010001.
Sonavane, G., Tomoda, K., Sano, A., Ohshima, H., Terada, H., Makino, K., 2008. In vitro permeation of gold nanoparticles through rat skin and rat intestine: Effect of particle size. Colloids Surfaces B Biointerfaces 65, 1–10. https://doi.org/10.1016/j.colsurfb.2008.02.013.
Sztandera, K., Gorzkiewicz, M., Klajnert-Maculewicz, B., 2019. Gold nanoparticles in cancer treatment. Mol. Pharm. 16, 1–23. https://doi.org/10.1021/acs.molpharmaceut.8b00810.
The Engineering ToolBox, 2003. Specific Heat of common Substances [WWW Document]. URL https://www.engineeringtoolbox.com/specific-heat-capacity-d_391.html (accessed 1.13.23).
Turkevich, J., Stevenson, P.C., Hillier, J., 1951. A study of the nucleation and growth processes in the synthesis of colloidal gold. Discuss. Faraday Soc. 11, 55–75. https://doi.org/10.1039/DF9511100055.
Urries, I., Muñoz, C., Gomez, L., Marquina, C., Sebastian, V., Arruebo, M., Santamaria, J., 2014. Magneto-plasmonic nanoparticles as theranostic platforms for magnetic resonance imaging, drug delivery and NIR hyperthermia applications. Nanoscale 6, 9230–9240. https://doi.org/10.1039/c4nr01588f.
Van Haute, D., Berlin, J.M., 2017. Challenges in realizing selectivity for nanoparticle biodistribution and clearance: lessons from gold nanoparticles. Ther. Deliv. 8, 763–774. https://doi.org/10.4155/tde-2017-0057.
Venditti, I., 2019. Engineered gold-based nanomaterials: Morphologies and functionalities in biomedical applications. a mini review. Bioengineering 6, 53. https://doi.org/10.3390/bioengineering6020053.
Wang, J., Drelich, A.J., Hopkins, C.M., Mecozzi, S., Li, L., Kwon, G., Hong, S., 2022. Gold nanoparticles in virus detection: Recent advances and potential considerations for SARS-CoV-2 testing development. Wiley Interdiscip. Rev. Nanomedicine Nanobiotechnology 14, e1754. https://doi.org/10.1002/wnan.1754.
Wang, S., Lu, W., Tovmachenko, O., Rai, U.S., Yu, H., Ray, P.C., 2008. Challenge in understanding size and shape dependent toxicity of gold nanomaterials in human skin keratinocytes. Chem. Phys. Lett. 463, 145–149. https://doi.org/10.1016/j.cplett.2008.08.039.
Wang, Q., Zhang, X., Sun, Y., Wang, L., Ding, L., Zhu, W.H., Di, W., Duan, Y.R., 2019. Gold-caged copolymer nanoparticles as multimodal synergistic photodynamic/photothermal/chemotherapy platform against lethality androgen-resistant prostate cancer. Biomaterials 212, 73–86. https://doi.org/10.1016/j.biomaterials.2019.05.009.

Xu, X., Chong, Y., Liu, X., Fu, H., Yu, C., Huang, J., Zhang, Z., 2019b. Multifunctional nanotheranostic gold nanocages for photoacoustic imaging guided radio/photodynamic/photothermal synergistic therapy. Acta Biomater. 84, 328–338. https://doi.org/10.1016/j.actbio.2018.11.043.

Xu, W., Wang, J., Qian, J., Hou, G., Wang, Y., Ji, L., Suo, A., 2019a. NIR/pH dual-responsive polysaccharide-encapsulated gold nanorods for enhanced chemo-photothermal therapy of breast cancer. Mater. Sci. Eng. C 103, 109854. https://doi.org/10.1016/j.msec.2019.109854.

Yang, Y., Gao, N., Hu, Y., Jia, C., Chou, T., Du, H., Wang, H., 2015b. Gold nanoparticle-enhanced photodynamic therapy: effects of surface charge and mitochondrial targeting. Ther. Deliv. 6 (3), 307–321.

Yang, W., Xia, B., Wang, L., Ma, S., Liang, H., Wang, D., Huang, J., 2021. Shape effects of gold nanoparticles in photothermal cancer therapy. Mater. Today Sustain. 13, 100078. https://doi.org/10.1016/j.mtsust.2021.100078.

Yang, X., Yang, M., Pang, B., Vara, M., Xia, Y., 2015a. Gold nanomaterials at work in biomedicine. Chem. Rev. 115, 10410–10488. https://doi.org/10.1021/acs.chemrev.5b00193.

Yano, T.-A., Kajisa, T., Ono, M., Miyasaka, Y., Hasegawa, Y., Saito, A., Otsuka, K., Sakane, A., Sasaki, T., Yasutomo, K., Hamajima, R., Kanai, Y., Kobayashi, T., Matsuura, Y., Itonaga, M., Yasui, T., 2022. Ultrasensitive detection of SARS-CoV-2 nucleocapsid protein using large gold nanoparticle-enhanced surface plasmon resonance. Sci. Rep. 12 (1) https://doi.org/10.1038/s41598-022-05036-x.

Yi, X., Duan, Q.-Y., Wu, F.-G., 2021. Low-temperature photothermal therapy: Strategies and applications. Research 2021, 1–38. https://doi.org/10.34133/2021/9816594.

Yuan, C., Wang, C., Wang, J., Kumar, V., Anwar, F., Xiao, F., Mushtaq, G., Liu, Y., Kamal, M.A., Yuan, D., 2016. Inhibition on the growth of human MDA-MB-231 breast cancer cells in vitro and tumor growth in a mouse xenograft model by Se-containing polysaccharides from Pyracantha fortuneana. Nutr. Res. 36, 1243–1254. https://doi.org/10.1016/j.nutres.2016.09.012.

Yun, S.H., Kwok, S.J.J., 2017. Light in diagnosis, therapy and surgery. Nat. Biomed. Eng. 1, 8. https://doi.org/10.1038/s41551-016-0008.

Zhang, R., Kiessling, F., Lammers, T., Pallares, R.M., 2023. Clinical translation of gold nanoparticles. Drug Deliv. Transl. Res. 13, 378–385. https://doi.org/10.1007/s13346-022-01232-4.

Zhang, L., Zhang, S., Chen, H., Liang, Y., Zhao, B., Luo, W., Xiao, Q., Li, J., Zhu, J., Peng, C., Zhang, Y., Hong, Z., Wang, Y., Li, Y., 2020. An acoustic/thermo-responsive hybrid system for advanced doxorubicin delivery in tumor treatment. Biomater. Sci. 8, 2202–2211. https://doi.org/10.1039/c9bm01794a.

Zhang, Y., Zhang, S., Zhang, Z., Ji, L., Zhang, J., Wang, Q., Guo, T., Ni, S., Cai, R., Mu, X., Long, W., Wang, H., 2021. Recent progress on NIR-II photothermal therapy. Front. Chem. 9, 1–26. https://doi.org/10.3389/fchem.2021.728066.

Zhou, C., Long, M., Qin, Y., Sun, X., Zheng, J., 2011. Luminescent gold nanoparticles with efficient renal clearance. Angew. Chemie - Int. Ed. 50, 3168–3172. https://doi.org/10.1002/anie.201007321.

Zou, L., Wang, H., He, B., Zeng, L., Tan, T., Cao, H., He, X., Zhang, Z., Guo, S., Li, Y., 2016. Current approaches of photothermal therapy in treating cancer metastasis with nanotherapeutics. Theranostics 6, 762–772. https://doi.org/10.7150/thno.14988.